Materials Advances

ROYAL SOCIETY OF CHEMISTRY

PAPER

View Article Online
View Journal | View Issue

Cite this: *Mater. Adv.*, 2025, 6, 2071

Semiconducting ferromagnetism and thermoelectric performance of Rb_2GeMI_6 (M = V, Ni, Mn): a computational perspective

Mudasir Younis Sofi, Mohd. Shahid Khan and M. Ajmal Khan*

We present a comprehensive first-principles investigation into the structural, electronic, magnetic, and transport properties of halide double perovskites Rb_2GeMI_6 (M = V, Mn, Ni) utilizing density functional theory (DFT). Structural stability is rigorously validated through geometric optimization, mechanical stability criteria, and tolerance factor analysis, confirming the feasibility of these compounds in the cubic $Fm\bar{3}m$ phase. Total energy calculations based on the Birch–Murnaghan equation of state establish a robust ferromagnetic ground state, further corroborated by positive Curie–Weiss constants of 98 K (Rb_2GeVI_6), 90 K (Rb_2GeMnI_6), and 95 K (Rb_2GeNiI_6), underscoring their intrinsic ferromagnetic behavior. Electronic structure analyses performed using both the generalized gradient approximation (GGA) and the Tran–Blaha modified Becke–Johnson (TB-mBJ) potential reveal that these materials exhibit semiconducting ferromagnetism, characterized by a significant spin-splitting gap. The underlying mechanism is traced to the crystal field effects influencing the d-orbitals of the transition metal atoms. Magnetic moment calculations indicate values of $3\mu_B$, $5\mu_B$, and $2\mu_B$ for the V-, Mn-, and Ni-based compounds, respectively, underscoring the pivotal role of transition metals in governing their magnetic properties. Furthermore, Curie temperature estimations of 530.39 K (Rb_2GeVI_6), 580.72 K (Rb_2GeMnI_6), and 440.47 K (Rb_2GeNiI_6) significantly exceed room temperature, reinforcing their potential for spintronic applications. A rigorous thermodynamic analysis, incorporating vibrational contributions to internal energy, Helmholtz free energy, entropy, and specific heat, confirms the stability of these materials across a broad temperature range. Finally, an in-depth investigation of transport properties, considering both temperature and chemical potential dependence of the Seebeck coefficient, electrical conductivity, and figure of merit (zT), highlights their exceptional thermoelectric potential. Notably, the materials exhibit remarkably low thermal conductivities of 3.10 W m^{-1} K^{-1} (Rb_2GeVI_6), 2.05 W m^{-1} K^{-1} (Rb_2GeMnI_6), and 1.57 W m^{-1} K^{-1} (Rb_2GeNiI_6), translating into impressive zT values of 1.00, 0.99, and 0.97 at room temperature. Overall, this study demonstrates that Rb_2GeMI_6 halide perovskites exhibit a unique synergy of structural stability, ferromagnetic semiconducting behavior, and high thermoelectric efficiency, positioning them as promising candidates for next-generation spintronic devices, thermoelectric energy harvesting, and sustainable energy technologies.

Received 30th October 2024,
Accepted 26th February 2025

DOI: 10.1039/d4ma01091d

rsc.li/materials-advances

1. Introduction

The progression of modern technology necessitates the optimization of information processing and storage with maximum efficiency. Future research in this domain is anticipated to focus on spintronics, which utilizes electron spin as an additional degree of freedom, distinguishing it from conventional charge-based electronics.[1,2] Compared to conventional electronics, spintronic devices promise lower power consumption, ultrafast operation, and non-volatility, making them essential for next-generation applications such as magnetoresistive random-access memory (MRAM), spin valves, and magnetic sensors.[3–5] The successful realization of spintronics, however, relies on the development of materials that exhibit both robust ferromagnetism and semiconducting behavior, known as magnetic semiconductors.[6] Over the years, various materials, including Eu- and Mn-based chalcogenide,[7–9] spinel oxides,[10,11] and Mn-doped II–VI and III–V semiconductors,[12–15] have been explored for their potential to integrate spin functionality with semiconductor properties. While these materials have demonstrated promising spin-dependent transport properties, their low Curie temperatures, weak spin polarization, and limited structural stability hinder their practical application. To overcome these limitations, researchers have turned their attention to perovskite-based materials, a class known for their structural tunability, strong electron correlation effects, and exceptional charge transport properties.[16] Within the perovskite family, oxide perovskites have

Department of Physics, Jamia Millia Islamia, New Delhi-110025, India.
E-mail: majkhan@jmi.ac.in

been widely studied for spintronic applications due to their well-established synthesis and integration into microelectronic devices. However, halide perovskites, initially investigated for their superior optoelectronic performance, have recently attracted significant interest as potential candidates for magnetic and spintronic applications.[17] The first indication of weak magnetism in Mn-doped methylammonium lead iodide ($CH_3NH_3PbI_3$) by Náfrádi *et al.*[18] provided early evidence of the feasibility of halide perovskites as magnetic semiconductors. Despite this breakthrough, their low Curie temperatures (<15 K), small spin splitting (<0.2 eV), and phase instability significantly limit their utility in practical spintronic devices. Given these challenges, there has been a growing interest in intrinsic magnetic semiconductors—materials that naturally exhibit ferromagnetism without external doping. In this context, double perovskite oxides (DPOs) have garnered attention due to their structural simplicity, tunable electronic states, and chemical versatility.[19] However, their halide counterparts, double perovskite halides (DPHs), remain largely unexplored, despite their potential to bridge the gap between structural stability and strong magnetic interactions. Recent studies, such as those by Cai *et al.*,[20] have demonstrated ferromagnetism in lead-free $Cs_2GeB'X_6$-type halide perovskites, opening new avenues for the development of stable, high-performance spintronic materials.

Beyond advancements in spintronics, the increasing global demand for sustainable energy solutions and efficient waste heat recovery has intensified the search for high-performance thermoelectric materials capable of directly converting heat into electricity. To date, a plethora of materials have been reported to exhibit promising thermoelectric performance;[21–25] however, many of them suffer from inherent limitations that hinder widespread practical application. Conventional inorganic thermoelectric materials, such as Bi_2Te_3 and PbTe,[21,22] demonstrate excellent efficiency but are burdened by high material costs, complex fabrication processes, and the scarcity or toxicity of constituent elements. Organic thermoelectric materials, while offering low-cost processing and mechanical flexibility, typically exhibit low power factors and poor long-term stability. Meanwhile, quantum dots and hybrid composites have shown potential for performance enhancement, yet their scalability and reproducibility remain significant challenges. Given these challenges, perovskites, including oxides and halides, have emerged as promising materials due to their tunable electronic properties and cost-effective processability.[26–29] While oxide perovskites have been extensively studied for thermoelectric applications,[26] halide perovskites have primarily been explored for their optoelectronic properties,[29] with limited focus on their thermoelectric potential, despite their inherently low thermal conductivity and efficient charge transport.[30] Since the first report of ultralow thermal conductivity in $CH_3NH_3PbI_3$,[31] extensive efforts have been directed toward understanding its thermal transport behavior, particularly phonon dynamics. Halide perovskites exhibit a unique "phonon glass, electron crystal" characteristic,[32] where charge carriers move efficiently like in high-quality semiconductors, while heat transport is significantly suppressed, resembling that of glassy materials.[33] Their high Seebeck coefficients and decent carrier mobilities further underscore their promise for thermoelectric applications, making them an exciting area for future exploration.[30,31] If stability challenges can be addressed, halide perovskites have the potential to bridge the gap between cost-effectiveness and high thermoelectric performance, positioning them as strong candidates for next-generation energy conversion technologies.

Despite the recent progress, the intricate relationship between magnetism, electronic structure, and thermoelectric performance in halide-based double perovskites remains largely unexplored. This study seeks to bridge this gap by conducting a comprehensive first-principles investigation into the structural stability, electronic properties, magnetic interactions, and thermoelectric performance of Rb_2GeMI_6 (M = V, Mn, Ni) halide perovskites using advanced density functional theory (DFT) and post-DFT methods. Notably, no prior research has systematically examined these materials within this context. The findings of our study disclose that halide-based double perovskites exhibit intrinsic ferromagnetic semiconductor behavior, characterized by substantial spin-splitting gaps, alongside high Curie temperatures and strong spin polarization, making them viable candidates for spintronic applications. Additionally, their favourable thermoelectric properties underscore their potential for efficient energy conversion technologies. By unveiling these critical attributes, this study positions halide-based double perovskites as a promising class of multifunctional materials for next-generation spintronic and thermoelectric devices.

This paper is organized to predict the comprehensive physical (structural, electronic, mechanical, phonon, thermodynamic) and thermoelectric properties of these materials.

2. Computational details

The present study employs the Wien2k software suite and its associated tools for computational analysis.[34] The Kohn–Sham equation is iteratively solved using the generalized gradient approximation (GGA).[35] However, since GGA often fails to accurately describe the electronic structures of systems with strongly correlated d-electrons, the Tran and Blaha modified Becke–Johnson (TB-mBJ, 2009) potential is applied on top of GGA, resulting in the GGA + mBJ method for improved accuracy.[36] The full-potential linearized augmented plane wave (FP-LAPW) method is used, with the computational domain divided into muffin-tin (MT) spheres centered at Wyckoff positions (4a, 4b, 8c, and 24e) to represent atomic sites, while the interstitial space accommodates the remaining volume. The radii of these MT spheres (RMT) are carefully chosen to balance charge leakage prevention and computational efficiency. Within these spheres, atomic-like wave functions are applied, whereas Bloch-like wave behavior is maintained in the interstitial regions. The angular momentum expansion inside the MT spheres extends up to l_{max} = 10, and the plane wave cutoff follows the condition $R_{MT} \times K_{max}$ = 7. The self-consistency criterion is defined by convergence requirements, ensuring that the integrated charge difference between consecutive iterations

remains below 0.0001e, while energy fluctuations do not exceed 0.0001 Ry. The electronic and magnetic structure calculations, along with elastic constant evaluations, are conducted using a Brillouin zone mesh comprising 1000 k-points. Mechanical stability is assessed using the Thomas Charpin cubic elastic package within the GGA–PBE framework.[37] Thermodynamic properties are determined using the Gibbs2 package,[38] integrated with the Wien2k software. Additionally, thermoelectric properties are computed based on Boltzmann transport theory, employing the rigid-band approximation and the constant-scattering time approximation (CSTA).[39] The Seebeck coefficient (S), electrical conductivity (σ), and electronic thermal conductivity (zT) are evaluated as functions of the chemical potential (μ) for the given perovskites, following established relationships:

$$S = \frac{ek_B}{\sigma}\int\left(-\frac{\partial f_0}{\partial \varepsilon}\right)\frac{\varepsilon-\mu}{k_B T}\Xi(\varepsilon)\mathrm{d}\varepsilon \quad (1)$$

$$\sigma = e^2\int\left(-\frac{\partial f_0}{\partial \varepsilon}\right)\Xi(\varepsilon)\mathrm{d}\varepsilon \quad (2)$$

$$\kappa_e = {k_B}^2 T\int\left(-\frac{\partial f_0}{\partial \varepsilon}\right)\left(\frac{\varepsilon-\mu}{k_B T}\right)^2\Xi(\varepsilon)\mathrm{d}\varepsilon. \quad (3)$$

Here, $\Xi(\varepsilon)$ is a transport distribution function specified by $\Xi^{\alpha,\beta}(\varepsilon) = \sum_k \delta(\varepsilon-\varepsilon_k)v_k^\alpha v_k^\beta \tau_k$ where v_k^α represent αth component of the group velocity with wave vector k. To enhance the accuracy of thermoelectric calculations, the k-mesh density has been increased to 100 000 k-points, ensuring precise transport property predictions.

3. Results and discussion

The physical properties of novel halide perovskites Rb_2GeMI_6 (M = V, Mn, Ni) are predicted using density functional theory (DFT) with PBE–GGA and TB-mBJ approximation schemes.

3.1 Structural and magnetic phase stability

To asesss the structural stability and feasibility of the given compounds, we employ the Goldschmidt tolerance factor (t_{dp}) and the octahedral factor (μ), both of which serve as fundamental criteria for predicting the formation and stability of a cubic perovskite framework. The stability of the cubic phase is validated through the calculation of the tolerance factor, which is defined as:[40] $t_{dp} = \frac{0.71(r_{Rb}+r_X)}{r_{avg}+r_X}$ where r_{Rb} and r_X represents the ionic radii of rubidium (Rb) and halide (I) atoms, respectively, while r_{avg} denotes the average ionic radius of the B-site cations, germanium (Ge) and transition metals M (V, Mn, Ni). The octahedral factor is given by:[40] $\mu = \frac{r_{avg}}{r_X}$. The calculated tolerance factor values for the studied materials range between 0.81 and 1.11, indicating structural stability in the $Fm\bar{3}m$ cubic phase. Additionally, the computed octahedral factor values ($0.29 \leq \mu \leq 0.55$) confirm the stability of the octahedral coordination, further supporting the cubic phase structure. Accordingly, a three-dimensional cubic

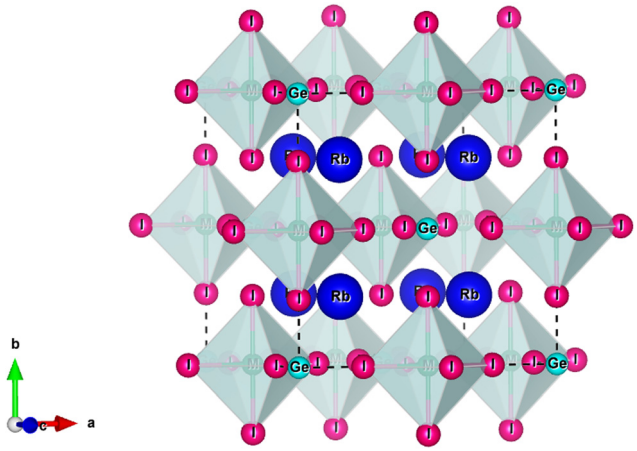

Fig. 1 Crystal structure of Rb_2GeMI_6 (M = V, Mn, Ni) double halide perovskites.

crystal structure is constructed, as illustrated in Fig. 1. Within the unit cell, rubidium (Rb) atoms occupy the A-site and are coordinated by twelve iodine (I) atoms, forming a cuboctahedra environment (Fig. 1). The B-site cations, Ge and M, are octahedrally coordinated by six iodine (I) anions, forming $[BX_6]$ octahedra, which are interconnected through shared anionic vertices. This octahedral network plays a crucial role in maintaining the structural integrity and electronic properties of the material.

Next, we investigate the magnetic phase stability of the studied compounds by simulating various magnetic configurations using the Birch–Murnaghan equation of state, given as:[41]

$$E(V) = E_0 + \frac{9B_0V_0}{16}\left\{\left[\left(\frac{V_0}{V}\right)^{2/3}-1\right]B_0' + \left[\left(\frac{V_0}{V}\right)^{2/3}-1\right]^2\left[6-4\left(\frac{V_0}{V}\right)^{2/3}\right]\right\}. \quad (4)$$

In this equation, $E(V)$ denotes the ground state energy, V represents the unit cell volume, and B_0 (B_0') corresponds to the bulk modulus (and its pressure derivative), respectively. The resulting energy *versus* volume curves for each magnetic configuration indicate that the ferromagnetic (FM) phase has the lowest energy, suggesting its favored stability compared to other magnetic states. Fig. 2 depicts the energy optimization for the FM phase (excluding other configurations for brevity), where the energy–volume curve exhibits a distinct minimum, corresponding to the optimal equilibrium volume. At this equilibrium volume, the lattice constants are determined to be 11.74 Å for Rb_2GeVI_6, 11.80 Å for Rb_2GeMnI_6, and 11.55 Å for Rb_2GeNiI_6, which are consistent with values reported in the literature.[20,40,42] The derived equilibrium parameters, obtained through total energy minimization, are summarized in Table 1. Furthermore, the lattice constants calculated using the generalized gradient approximation with the Perdew–Burke–Ernzerhof (GGA–PBE) functional exhibit excellent agreement with both theoretical predictions and experimental measurements, thereby reinforcing the validating of our results.

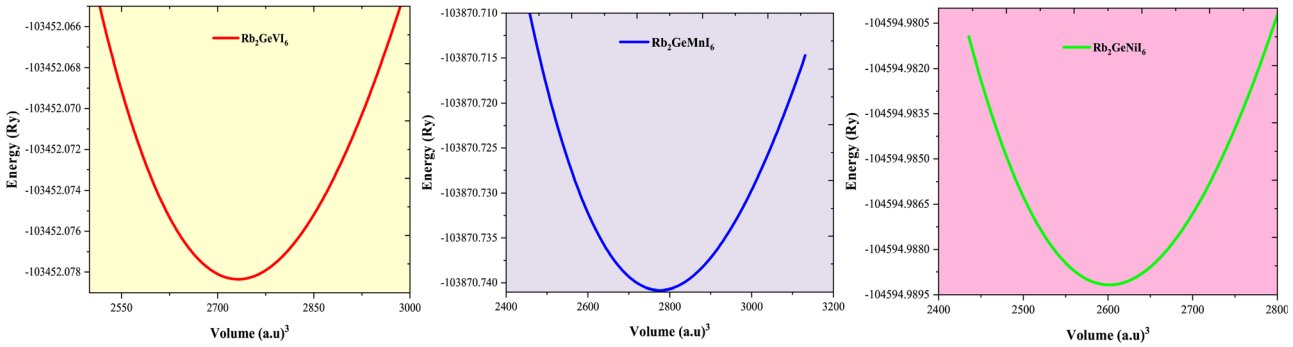

Fig. 2 Plot of the total energy against unit cell volume for Rb_2GeMI_6 (M = V, Mn, Ni,) determined *via* GGA–PBE functional scheme.

To evaluate the feasibility of synthesizing the given compounds and to predict their thermodynamic stability, the enthalpy of formation (ΔH) is determined using density functional theory (DFT) calculations. The expression employed for these calculations is given as:[42]

$$\Delta H = \frac{1}{10}\left[E_{\text{total}}^{Rb_2GeMI_6} - (2E_{Rb} + E_{Ge} + E_M + 6E_I)\right] \quad (5)$$

where $E_{\text{total}}^{Rb_2GeMI_6}$ represents the equilibrium energy of the unit cell, and E_{Rb} + E_{Ge} + E_M + $6E_I$ represent the DFT-calculated energies of rubidium (Rb), germanium (Ge), transition metal (M = V, Mn, Ni), and iodine (I) in their stable elemental crystalline forms. The calculated enthalpy values, summarized in Table 1, reveal negative formation enthalpies, implying that these materials are thermodynamically stable and synthetically viable.

To further confirm the robustness of the given compounds, cohesive energy (ΔE) is evaluated. This metric provides insight into the degree of interatomic bonding and structural stability of these materials. The cohesive energy is defined as:[42]

$$E_{\text{Coh}}^{Rb_2GeMI_6} = [2E_{Rb} + E_{Ge} + E_M + 6E_I] - E_{\text{total}}^{Rb_2GeMI_6} \quad (6)$$

where $E_{\text{total}}^{Rb_2GeMI_6}$ is the equilibrium energy of the unit cell, and E_{Rb}, E_{Ge}, E_M, and E_I are the energies of the isolated atoms Rb, Ge, M (V, Mn, Ni), and I, respectively. The computed cohesive energies, which are strictly positive (Table 1), further validate the interatomic binding strength and structural integrity of the compounds. High cohesive energy values indicate strong interactions among constituent atoms, minimizing the risk of spontaneous decomposition.

To support experimental efforts in material synthesis, simulated X-ray diffraction (XRD) patterns are generated using DFT calculations. The simulated diffraction spectra for Rb_2GeMI_6 compounds are obtained assuming a cubic crystal structure with an $Fm\bar{3}m$ space group symmetry (Fig. 3). The characteristic peak positions and intensities derived from these theoretical XRD patterns serve as reference data for experimental validation, aiding in phase identification and structural characterization.

3.2 Vibrational thermodynamic properties

The study of vibrational thermodynamic functions provides critical insights into the temperature dependence of various properties, including vibrational internal energy (E), vibrational Helmholtz free energy (A), vibrational entropy (S_V), and specific heat at constant volume (C_V). These properties play a fundamental role in understanding the thermodynamic behavior of materials. A widely used approach for modelling vibrational contributions is the quasi-harmonic Debye model,[43,44] which accounts for the influence of volume and temperature on vibrational states. Within this framework, the expressions governing key thermodynamic properties are as follows:

Vibrational Helmholtz free energy (A)

$$A_{\text{Vib}}\left(\theta(V); T = nk_BT\frac{9\theta_D}{8T} + 3\ln 1 - e^{\frac{\theta_D}{T}} - D\left(\frac{\theta_D}{T}\right)\right. \quad (7)$$

Debye temperature (θ_D)

$$\theta_D = \frac{h}{K_B}\left(6\pi^2 V^{\frac{1}{2}}N\right)^{\frac{1}{3}} f(v)\sqrt{\frac{B_s}{M}} \quad (8)$$

Vibrational entropy (S_V):

$$S_V = nk_BT\left[4D\left(\frac{\theta_D}{T}\right) - 3\ln 1 - e^{\frac{\theta_D}{T}}\right] \quad (9)$$

Table 1 Computed values for the optimised lattice parameter (a_0 in Å), bulk modulus (B in GPa), pressure derivative of bulk modulus, ground state energy (E_0 in Ry), tolerance factor (t_{dp}), octahedral factor (μ) enthalpy of formation (ΔH) and cohesive energy (E_C) of Rb_2GeMI_6 halide perovskites

Configuration	Phase	a_0	Previous works	B	B'_0	E_0	t_{dp}	μ	ΔH	E_C
Rb_2GeVI_6	FM	11.74	11.89[20] 11.85[27]	19.74	4.56	−103452.07	0.94	0.35	−1.25	20.12
Rb_2GeMnI_6	FM	11.80	11.92[20] 11.75[42]	20.38	3.81	−103870.74	0.96	0.32	−1.19	22.52
Rb_2GeNiI_6	FM	11.55	11.67[20] 11.48[40]	20.10	4.55	−104594.98	0.95	0.33	−1.14	19.19

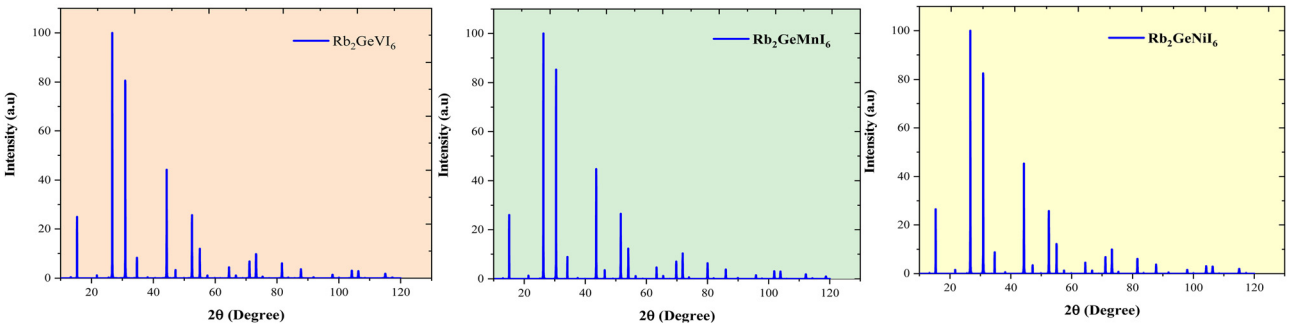

Fig. 3 DFT-simulated XRD patterns of Rb_2GeMI_6 (M = V, Mn, Ni) halide perovskites.

Specific heat at constant volume (C_V):

$$C_V = 3nk\left(4D\frac{\theta_D}{T} - \frac{3\theta_D/T}{e\theta_D/T}\right) \quad (10)$$

In these expressions, n denotes the number of atoms per formula unit, k_B is the Boltzmann constant, and D refers to the Debye integral, while B_s represents the adiabatic bulk modulus, M is the molecular mass per unit cell.

The temperature dependence of these functions provides valuable information about lattice dynamics and thermal properties of materials. By analyzing variations in vibrational internal energy, Helmholtz free energy, entropy, and heat capacity with temperature, it becomes possible to predict material behavior under different thermodynamic conditions.

Vibrational internal energy (E) exhibits a direct correlation with temperature (T), primarily due to the continuous absorption of thermal energy, which enhances atomic kinetic energy and increases vibrational amplitudes. The temperature-dependent evolution of vibrational internal energy (E), as illustrated in Fig. 4(a), exhibits a linear increase with temperature (T), signifying a proportional enhancement in the system's enthalpy. This linearity further implies that system enthalpy also rises proportionally with increasing temperature, reinforcing the direct contribution of vibrational excitations to the overall thermodynamic state of the material.

The Helmholtz free energy (A), depicted in Fig. 4(b), exhibits a decreasing trend with increasing temperature. This decline is observed across all considered compounds, signifying that the thermal energy available for useful work diminishes as T rises. The uniformity of this behavior suggests that variations in the

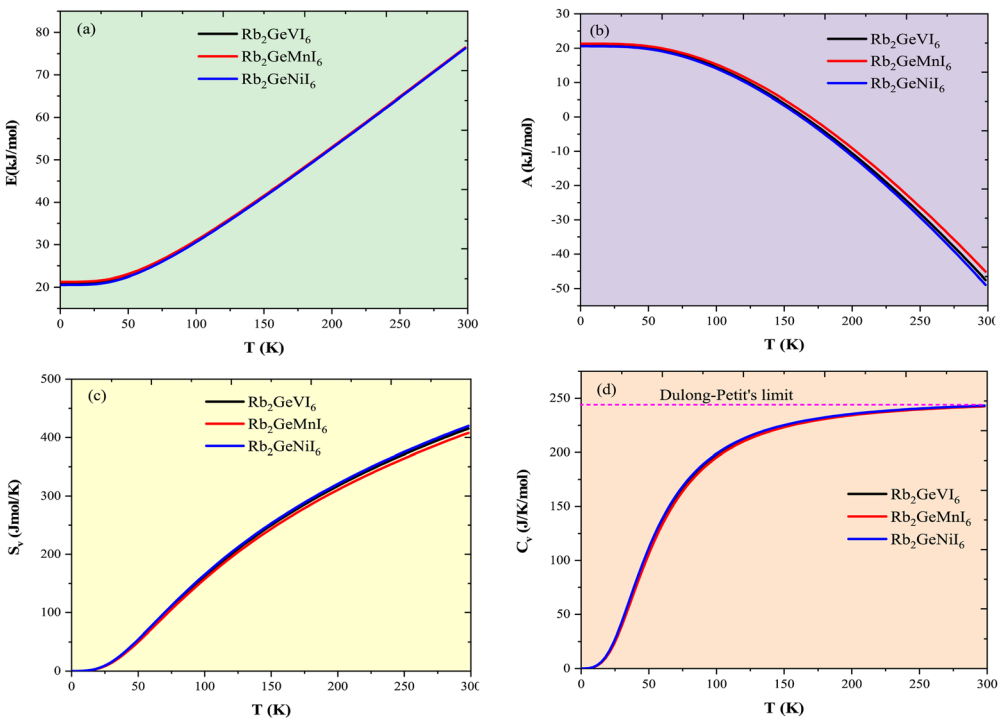

Fig. 4 Thermodynamic vibrational functions for Rb_2GeMI_6 (M = V, Mn, Ni) halide perovskites against selected range temperature (a) vibrational internal energy (E), (b) vibrational Helmholtz free energy (A), (c) vibrational entropy (S_v) and (d) specific heat (C_V).

transition metal have a minimal impact on the overall vibrational structure, as the halide ion remains unchanged. Since the vibrational internal energy is fundamentally governed by the phonon spectrum, comprising both acoustic and optical modes, the preservation of the halide ion ensures the stability of the primary lattice vibrations. While differences in transition metal properties influence local vibrational frequencies through changes in atomic mass and bond stiffness, the broader phonon density of states remains relatively unaffected. Consequently, Helmholtz free energy trends remain consistent across the series, indicating that global vibrational characteristics are largely dictated by the halide lattice framework.

Vibrational entropy (S_V), a measure of configurational and vibrational disorder, follows a systematic temperature-dependent increase, as shown in Fig. 4(c). Across all studied compounds, S_V exhibits similar behavior, with only marginal variations, further supporting the dominant role of the halide ion in maintaining lattice stability. The limited influence of the transition metal substitution on entropy arises from its minor effect on the overall vibrational spectrum, ensuring that the density of accessible vibrational states remains largely unchanged. The observed increase in S_V with rising temperature reflects the expansion of accessible vibrational states, leading to enhanced phonon population and greater configurational disorder. This temperature-dependent growth in vibrational entropy is consistent with the fundamental principles of statistical thermodynamics, where higher thermal energy levels facilitate broader phonon excitation and distribution.

In thermodynamics and statistical analysis,[45,46] heat capacity (C_V) plays a crucial role in examining the vibrational dynamics of lattice structures. The temperature dependence of C_V follows two distinct regimes, as shown in Fig. 4(d). At low temperatures ($T \ll \theta_D$), C_V follows Debye's model, exhibiting a cubic dependence on temperature: $C_V = \frac{12}{5}\pi^4 nR - \left(\frac{T}{\theta_D}\right)^3$. This arises because only long-wavelength acoustic phonons contribute significantly to heat capacity at low T. In contrast, at high temperatures ($T \gg \theta_D$), C_V approaches the Dulong–Petit limit:[47] $C_V \cong 3nR$ where R is the universal gas constant (8.314 J mol^{-1} K^{-1}). This occurs because, at such temperatures, all phonon modes are fully excited, and energy equipartition ensures that each degree of freedom contributes equally, resulting in a constant heat capacity. Table 2 presents the calculated Debye temperature (θ_D), zero-point energy (E_0 in kJ mol^{-1}), and Grüneisen parameter (γ), with comparisons to literature values that confirm the accuracy of our results.

The computed heat capacity profiles for Rb_2GeMnI_6 (M = V, Mn, Ni), illustrated in Fig. 4(d), conform to the above-mentioned regimes. At low temperatures, C_V follows a T^3 dependence, confirming Debye's law, while at higher T, it flattens toward the Dulong–Petit limit, reinforcing the accuracy of our computational outcomes with the classical thermodynamics.[47] The Debye temperatures (θ_D) listed in Table 2 show minimal variation across compounds, attributed to the conserved crystal structure and bonding environment due to the constant halide ion. Substituting the transition metal primarily affects atomic mass without significantly altering phonon spectra, resulting in nearly identical θ_D values. Furthermore, anharmonic effects are analyzed using the Grüneisen parameter (γ), defined as $\gamma = \frac{3(1+\varepsilon)}{2(2-\varepsilon)}$. The uniform values of γ across the compounds suggest a consistent thermal response, reinforcing the dominant role of the halide lattice in governing vibrational thermodynamics in Rb_2GeMnI_6 perovskites.

Table 2 Computed values for the Debye temperature (θ_D) measured in Kelvin, zero point energy (E_0) expressed in kilojoules per mole, and the Gruneisen parameter (γ) (dimensionless)

Parameter	θ_D	E_0	γ
Rb_2GeVI_6	222	20	2.00
Rb_2GeMnI_6	230	21	1.80
Rb_2GeNiI_6	220	20	2.17
K_2GeMnI_6[42]	230	21	2.10
K_2GeNiI_6[40]	230	23	2.03

3.3 Phonon stability

The vibrational stability and phonon transport characteristics of crystalline solids depend on their phonon dispersion behavior. Using density functional perturbation theory (DFPT) within the Quantum Espresso framework,[48] this study examines the phonon spectra to determine dynamic stability of the given perovskites. A material remains stable when all phonon frequencies are real and positive throughout the Brillouin zone, while negative (imaginary) frequencies indicate instability. The phonon dispersion curves in Fig. 5 show no imaginary modes, confirming the structural integrity of the studied materials. Each primitive unit cell contains ten atoms, resulting in three acoustic and twenty-seven optical phonon modes. At the Γ-point, the longitudinal acoustic (LA) and transverse acoustic (TA) phonons converge to zero frequency, as expected for stable crystalline lattices. The optical phonon modes, which include Raman-active, infrared-active, and silent branches, exhibit finite frequencies and contribute less significantly to heat transport. The phonon group velocity, defined as $v_g = \frac{d\omega}{dk}$, determines the efficiency of heat conduction by representing the slope of the phonon dispersion branches. A steeper slope corresponds to a higher group velocity, enabling faster phonon propagation and greater thermal conductivity. Acoustic modes, particularly the longitudinal acoustic (LA) branch, exhibit a near-linear dispersion with a significant slope, making them the dominant contributors to heat transport. In contrast, optical modes display flatter dispersion curves, resulting in lower group velocities and minimal contributions to thermal conduction. The material's thermal transport properties, therefore, primarily depend on the behavior of the acoustic phonons, which govern its potential applications in thermal engineering and thermoelectric devices.

3.4 Mechanical stability

The mechanical stability of a material is inherently tied to its atomic arrangement, which dictates its ability to resist external forces. This structural integrity determines its suitability for

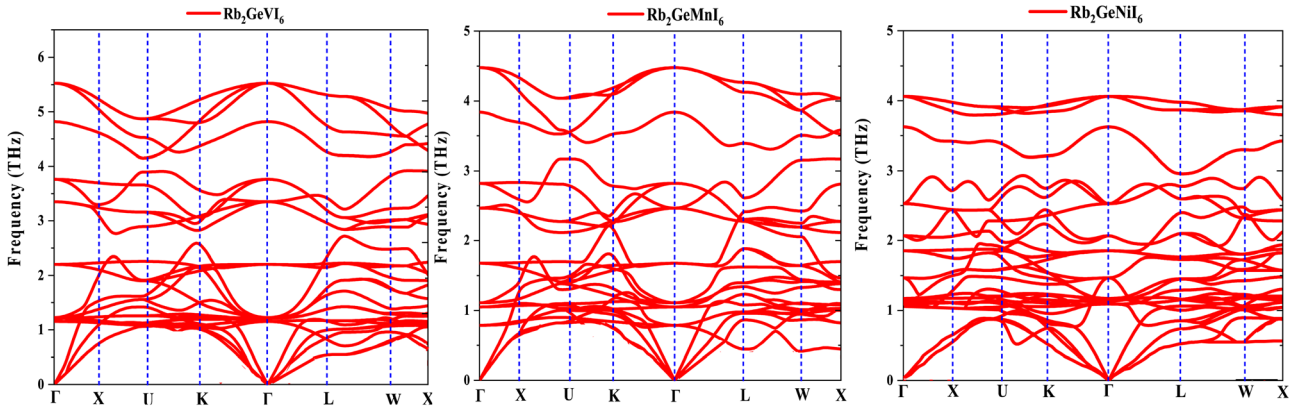

Fig. 5 Phonon band structure of Rb_2GeMI_6 (M = V, Mn, Ni) halide perovskites.

various technological and industrial applications. Understanding these properties requires an in-depth examination of how the material deforms and responds to mechanical stress. To assess the mechanical stability of Rb_2GeMI_6 halide perovskites, elastic constants are calculated using the energy–strain method, incorporating tetrahedral and rhombohedral distortions within the cubic elastic framework.[37] The results presented in Table 3 illustrates that all elastic constants are positive and comply with Born's stability criteria[49] ($C_{11} > 0$, $C_{12} > 0$, $C_{44} > 0$, and $C_{11} + 2C_{12} > 0$), thereby substantiating the mechanical stability of the compounds. By analyzing the elastic constants, we obtain essential mechanical parameters, including bulk, shear, and Young's moduli, which clarify the material's response to stress.[50–53] The bulk modulus (B), which quantifies resistance to uniform compression, is inversely related to volumetric deformation, influencing the material's ability to withstand structural collapse. The shear modulus (G) describes resistance to shape deformation, where lower values indicate greater plasticity and flexibility. Young's modulus (Y), a fundamental measure of stiffness, reveals the material's ability to resist elongation under tensile stress. The computed values follow the trend $Y > B > G$, indicating that these perovskites resist shape deformation more than volumetric changes, showcasing their structural rigidity and resilience. The ability of these materials to resist bond bending and angular distortions is evaluated through the Kleinman coefficient (ζ).[53] A lower value of ζ signifies a stronger preference for bond stretching over angular distortion, suggesting that these perovskites maintain their structural integrity even under stress.

Ductility and brittleness are key mechanical properties that define how a material deforms under external forces. To classify these perovskites, several mechanical indicators are examined, including Cauchy's pressure, Pugh's ratio, and Poisson's ratio.[53–55] A positive Cauchy's pressure indicates a ductile nature, while negative values suggest brittleness. Pugh's ratio, which is the ratio of the bulk modulus to the shear modulus (B/G), serves as another critical measure, where values greater than 1.75 classify a material as ductile. Poisson's ratio (ν) further supports this classification, as values above 0.26 are characteristic of ductile materials, while lower values imply brittleness. The computed values, summarized in Table 3, consistently confirm that Rb_2GeMI_6 perovskites exhibit strong ductile behavior, making them suitable for applications requiring mechanical flexibility, toughness, and resistance to fracture.

The mechanical behavior of crystalline materials is often influenced by their anisotropy, which determines variations in mechanical responses along different crystallographic directions. To assess the anisotropic character in Rb_2GeMI_6 halide perovskites, we evaluate two key anisotropy parameters: the Zener anisotropy ratio (A_Z) and the Universal anisotropic factor (A_U) using the expressions as:[56,57] $A_Z = \frac{2C_{44}}{C_{11} - C_{12}}$, $A_U = 5\frac{G_V}{G_R} - 5$, where the symbols have their usual meanings. These parameters provide insight into the deviation from isotropic behavior, where $A = 1$ represents a perfectly isotropic material. The results, presented in Table 3, indicate significant anisotropy in the studied compounds, as reflected in the deviation of both A_Z and A_U from unity. This anisotropic nature suggests that the mechanical response of these perovskites varies with direction, which could influence their structural applications.

Beyond anisotropy, evaluating mechanical constants enables the estimation of critical dynamic properties such as

Table 3 Intended second order elastic constants C_{11}, C_{12}, and C_{44} (GPa); bulk modulus B (GPa); shear modulus G (GPa) Young's modulus Y (GPa); Poisson's ratio ν; B/G ratio; Cauchy's pressure ($C_{12} - C_{44}$), Kleiman's parameter (ξ), Zener anisotropic constant (A_Z) and universal anisotropic constant (A_U) for Rb_2GeMI_6 double halide perovskites

Parameter	C_{11}	C_{12}	C_{44}	B	G	Y	ν	B/G	C_{12}–C_{44}	ξ	A_Z	A_U
Rb_2GeVI_6	27.21	11.23	7.12	16.55	7.45	19.44	0.30	2.22	4.11	0.54	0.89	0.016
Rb_2GeMnI_6	32.44	12.79	6.03	19.34	7.33	19.54	0.33	2.63	6.76	0.53	0.61	0.29
Rb_2GeNiI_6	34.58	12.98	7.98	20.18	9.00	23.52	0.30	2.23	5.01	0.51	0.73	0.11

average sound velocity (V_{av}). This parameter, which reflects the propagation of acoustic waves within a material, is derived from the transverse (V_t) and longitudinal (V_l) sound velocities using density-dependent relations:[53] $V_t = \sqrt{\frac{G}{\rho}}$ and $V_l = B = \sqrt{\frac{(3B+4G)}{3\rho}}$, where ρ represents the material's density. The average sound velocity (V_{av}) is then determined using the expression:[53] $V_{av} = \left[\frac{1}{3}\left(\frac{1}{3}\frac{2}{v_t^3} + \frac{1}{v_l^3}\right)\right]^{-\frac{1}{3}}$. Table 4 illustrates a clear decrease in V_{av} from the V-based compound to the Ni-based one, a trend that correlates with the progressive increase in density (V > Mn > Ni). The observed variations in sound velocity are critical for applications in phononic and thermoelectric materials, where acoustic wave interactions play a vital role in energy transport.

To further explore the mechanical resilience and industrial feasibility of these perovskites, we compute additional material parameters, including Vickers hardness (H_V), machinability factor (μ_m), Frantsevich's ratio (G/B), and melting temperature (T_m), using empirical relations from the literature:[53,58–61]

$$(H_V)_{Teter} = 0.151G, \quad (H_V)_{Tian} = 0.92\,(G/B)^{1.137}G^{0.708} \tag{11}$$

$$\mu_m = \frac{B}{C_{44}} \tag{12}$$

$$T_m\,(K) = [553\,(K) + (5.911)C_{11}]GPa \pm 300 \tag{13}$$

The hardness values, estimated using the models proposed by Teter *et al.*[58] and Tian *et al.*,[59] consistently produce positive results across all examined materials, indicating their intrinsic resistance to plastic deformation. Meanwhile, the machinability factor (μ_m) suggests that these perovskites possess favourable machining characteristics, including reduced cutting forces and mild lubricating properties, which are beneficial for industrial processing.

Another crucial parameter, melting temperature (T_m), is estimated using a correlation involving elastic stiffness constants. The high T_m values obtained reinforce the thermal stability of these compounds, positioning them as viable candidates for high-temperature applications. Furthermore, the relatively small G/B ratio suggests that these materials exhibit a balance between stiffness and plasticity, which is essential for structural durability. Collectively, the data compiled in Table 4, comprising high Vickers hardness, favourable machinability, elevated melting temperatures, and a relatively small G/B ratio, demonstrate that these materials might be promising candidates for advanced thermoelectric applications, especially under high-temperature conditions. Overall, the combination of strong anisotropy, high hardness, favourable machinability, and superior thermal stability underscores the potential of Rb_2GeMI_6 perovskites for advanced technological applications.

Table 4 Computed values of transverse (V_t in m s^{-1}), longitudinal (V_l in m s^{-1}) and average sound velocity (V_{av} in m s^{-1}), Frantsevich's ratio (G/B), machinability factor (μ_m) (unitless), Vickers hardness (H_V) (unitless), and melting temperature (T_m in K) for Rb_2GeMI_6 perovskites

Parameter	V_t	V_l	V_{av}	G/B	μ_m	$(H_V)_{Teter}$	$(H_V)_{Tian}$	$T_m \pm 300$
Rb_2GeVI_6	1311	2471	2335	0.45	2.32	1.12	1.54	713.83
Rb_2GeMnI_6	1308	2607	2044	0.38	3.20	1.08	1.25	744.75
Rb_2GeNiI_6	1436	2716	1925	0.44	2.52	1.36	1.74	757.40

3.5 Electronic structure

The electronic profile of Rb_2GeMI_6 (M = V, Mn, Ni) halide perovskites is systematically investigated through spin-polarized band structure (BS) and density of states (DOS) calculations. The band structures, computed using both GGA and GGA + mBJ approximations, are systematically analyzed and presented in Fig. 6(a)–(c). The GGA-derived band structure shows an unoccupied Fermi level in both spin orientations, with the up-spin channel grazing the valence band maximum, while the spin-down counterpart remains completely unoccupied. This confirms the presence of a finite band gap in both spin states, a hallmark of ferromagnetic semiconducting behavior. The band gap, a fundamental determinant of electronic transitions, is systematically evaluated using both computational frameworks. While GGA tends to underestimate band gaps due to the intricate correlation effects of d-electrons in transition metals, the mBJ correction refines these estimations, yielding values in strong agreement with prior literature,[20,40,42] as tabulated in Table 5. A refined analysis of the energy band dispersion reveals a stark contrast between spin channels. The spin-up states exhibit significant delocalization, leading to a reduced charge carrier effective mass and enhanced transport properties. In contrast, the spin-down states are more localized, resulting in a higher effective mass, which directly impacts carrier mobility and conductivity. This disparity in effective mass plays a crucial role in enhancing the transport dynamics of these compounds.

Beyond the conventional band gap analysis, the spin splitting gap, defined as the energy difference between the valence band maximum (VBM) or conduction band minimum (CBM) and the Fermi level across both spin states, is quantitatively evaluated. The computed spin splitting values, summarized in Table 5, are substantial and align well with those of similar materials,[20,40,42] highlighting the intrinsic potential of these halide perovskites for spintronic applications. The strong spin polarization and band engineering flexibility make these materials promising for next-generation spintronic applications.

3.5.1 Density of states. The electronic properties of Rb_2GeMI_6 (M = V, Mn, Ni) perovskites can be comprehensively analyzed through density of states (DOS) and partial density of states (PDOS) calculations, as illustrated in Fig. 7. These plots, obtained using the GGA + mBJ method, further validate the ferromagnetic semiconducting nature of these compounds, in strong agreement with the corresponding band structures. A detailed examination of the atomic contributions to the electronic structure reveals that the upper valence band is primarily dominated by the halogen (I) states, while the conduction band is largely shaped by the transition metal (M = V, Mn, Ni) d-states. These d-states, which undergo splitting into t_{2g} and e_g sub-bands, play a crucial role in governing the overall electronic behavior of these materials. To further understand the origin of the semiconducting nature observed in these double perovskites, it is essential to explore the crystal field effects

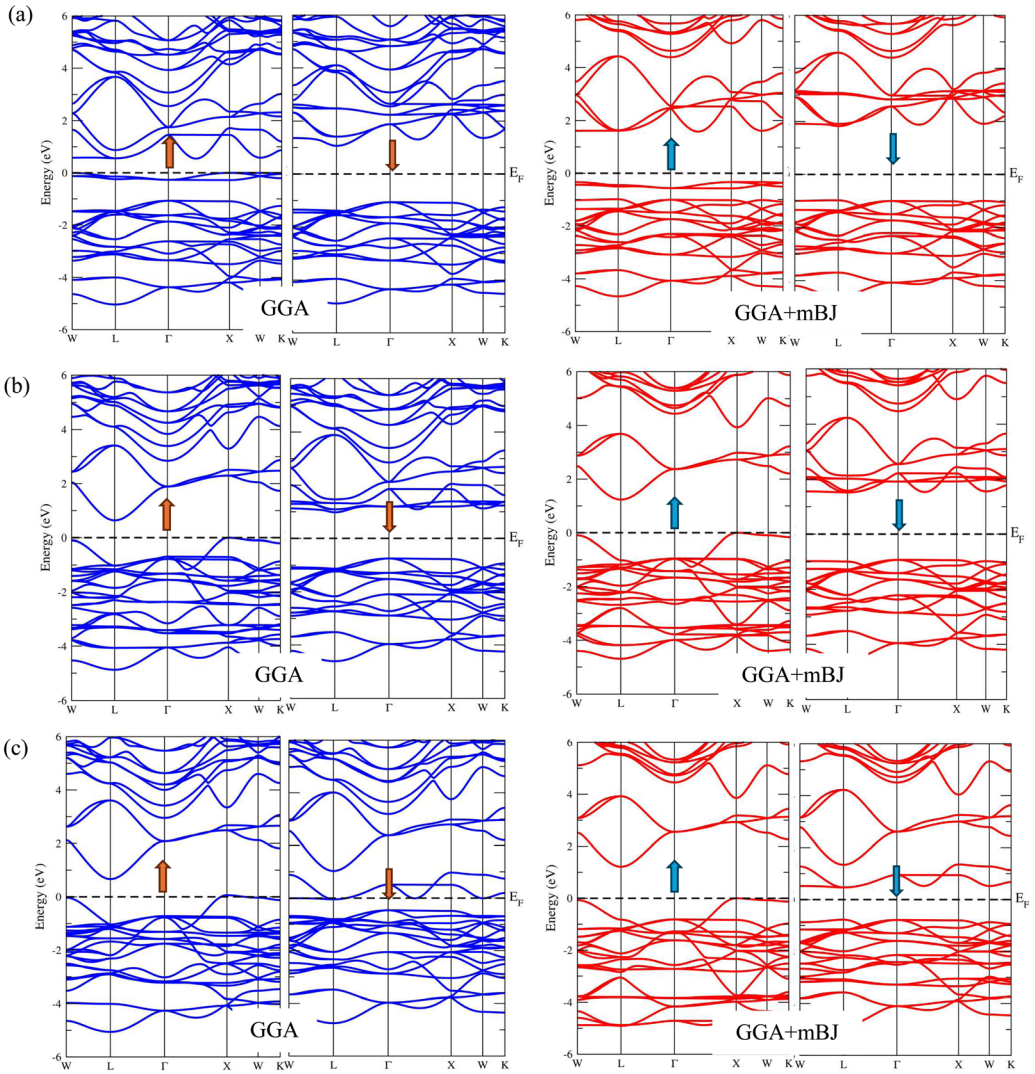

Fig. 6 DFT executed spin polarised band structure of (a) Rb_2GeVI_6, (b) Rb_2GeMnI_6, and (c) Rb_2GeNiI_6 halide perovskites calculated *via* GGA and GGA + mBJ approximations. The upward arrow represents the spin-up channel, while the downward arrow signifies the spin-down channel.

Table 5 Illustrated values of the band gap (eV) and spin-splitting gap (eV), determined *via* GGA and GGA + mBJ approximations for Rb_2GeMI_6 perovskites

Parameter	Band gap				Spin-splitting gap			
Approximation	GGA		GGA + mBJ		GGA		GGA + mBJ	
Spin channel	Up	Down	Up	Down	ΔE_{CBM}	ΔE_{VBM}	ΔE_{CBM}	ΔE_{VBM}
Rb_2GeVI_6	0.35	2.09	1.86	2.76	−0.73	0.85	−0.25	0.64
Rb_2GeMnI_6	0.61	1.70	1.22	2.41	−0.34	0.74	−0.33	0.92
Rb_2GeNiI_6	0.88	0.46	1.19	1.22	0.88	0.46	0.74	0.77
Cs_2GeVI_6[20]	—	—	—	—	—	—	−0.21[a]	0.01[a]
K_2GeMnI_6[42]	0.61	1.71	1.21	2.45	−0.34	0.78	−0.32	0.98
K_2GeNiI_6[40]	—	—	1.16	1.22	—	—	0.72	0.79

[a] These results were computed using the GGA + U_{eff} method, as reported by Cai *et al.*[20]

responsible for d-orbital splitting. For Rb_2GeMI_6 perovskites, the transition metal (V, Mn, Ni) resides at the centre of an octahedral coordination environment formed by six surrounding iodine (I) ligands. This ligand arrangement generates an electrostatic field around the metal ion, which alters the energy levels of the d-orbitals. In an idealized spherical field, all five d-orbitals experience an upward energy shift due to electrostatic repulsion. However, due to the specific geometry of the octahedral coordination, this repulsion is not uniform. The orbitals oriented directly along the Cartesian axes ($d_{x^2-y^2}$ and d_{z^2})

experience greater repulsion, leading to an increase in their energy, while the orbitals oriented between the axes (d_{xy}, d_{yz}, d_{zx}) experience a lower energy shift. As a result, the d-orbitals split into two sets: the lower-energy triply degenerate t_{2g} states and the higher-energy doubly degenerate e_g states. In an octahedral complex, the degree of separation between the d-t_{2g} and d-e_g orbitals is represented by Δ_o, known as the octahedral crystal field splitting energy. The electron distribution within these orbitals follows a specific pattern, with the d-t_{2g} set accommodating six electrons ($3\uparrow$, $3\downarrow$) and the d-e_g set holding four electrons ($2\uparrow$, $2\downarrow$), maintaining the total capacity of 10 electrons in d-orbitals. The arrangement of these electrons determines whether the complex adopts a high-spin or low-spin configuration, which is influenced by the strength of the crystal field splitting and the nature of the ligands, whether they are weak-field or strong-field, interacting with the central metal ion. The electronic configuration and spin state of the transition metal ion (V, Mn, Ni) within $Rb_2^{+1}Ge^{+2}M^{+2}I_6^{-1}$ are further dictated by crystal field splitting and ligand strength. Given that iodine (I) is a weak field ligand, the resulting crystal field splitting is relatively small. Consequently, the electrons prefer to occupy orbitals according to Hund's rule, favouring high-spin configurations that maximize unpaired electrons. In contrast, strong field ligands induce a much larger crystal field splitting, leading to a low-spin electronic configuration where electrons occupy the lower-energy t_{2g} orbitals before populating the e_g states. For V-based compound, the electron filling in the d-orbitals will be $3t_{2g}$ ($\uparrow$), $0e_g$ ($\uparrow$), $0t_{2g}$ ($\downarrow$), and $0e_g$ ($\downarrow$). Here, the d-t_{2g} orbitals are fully occupied with one electron each in the up-spin state, contributing to the valence band (VB), while the d-e_g states in spin-up state and d-t_{2g} orbitals in the down-spin state are empty, forming the conduction band (CB), which accordingly demonstrates the semiconducting nature of Rb_2GeVI_6 compound. For the manganese (Mn) based compound, Mn^{2+} has an electron configuration of $3t_{2g}$ ($\uparrow$), $2e_g$ ($\uparrow$), $0t_{2g}$ ($\downarrow$), and $0e_g$ ($\downarrow$). The d-t_{2g} and d-e_g orbitals have one electron each in the up-spin state, while the down-spin state remains empty. Thus, the energy levels of Mn-d-t_{2g} and Mn-d-e_g contribute to the VB, and the empty states in the down-spin configuration reside in the CB, thereby establishing the semiconducting characteristics Rb_2GeMnI_6 perovskite. For Rb_2GeNiI_6, the d-t_{2g} orbitals are fully occupied in both spin-up and spin-down states, while d-e_g orbitals are half-filled. The empty d-e_g orbitals in the spin-down state define the CB minima, illustrating the semiconducting properties of Rb_2GeNiI_6. Consequently, the inherent semiconducting nature of these halide perovskites, combined with their favourable bandgap, points to their potential utility in a range of optical applications. Their ability to efficiently manage exciton recombination makes them promising candidates for active layers in devices such as light-emitting diodes (LEDs) and semiconductor lasers.

Table 6 Calculated values of spin magnetic moments of mixed charge density for Rb_2GeMI_6 (M = V, Mn, Ni) compounds using TB-mBJ approximations

Material	Method	Rb (μ_B)	Ge (μ_B)	M (μ_B)	I (μ_B)	Interstitial (μ_B)	Total (μ_B)
Rb_2GeVI_6	GGA + mBJ	0.00	−0.00	2.71	0.00	0.25	3.00
Rb_2GeMnI_6	GGA + mBJ	0.00	0.06	4.55	0.02	0.22	5.00
Rb_2GeNiI_6	GGA + mBJ	0.00	0.08	1.60	0.03	0.08	2.00

3.5.2 Magnetism and Curie temperature. Next, we investigate the magnetic properties of Rb_2GeMI_6 alloys (M = V, Mn, Ni) using multiple approximation techniques, with a particular focus on the Trans Blaha modified Becke Johnson (TB-mBJ) method. This approach is well suited for accurately capturing the intricate electronic interactions that dictate the magnetic behavior of these materials. The spin magnetic moments, both total and partial, computed through the TB-mBJ method are presented in Table 6. The results obtained using the GGA + mBJ approximation reveal total magnetic moments of $3\mu_B$ for Rb_2GeVI_6, $5\mu_B$ for Rb_2GeMnI_6, and $2\mu_B$ for Rb_2GeNiI_6. These values can be explained by the lattice structures of these compounds, which support 3, 5, and 2 unpaired spins respectively, corresponding to the observed magnetism of $3\mu_B$, $5\mu_B$, and $2\mu_B$. The electronic configurations for the transition metals M (V, Mn, Ni) in these compounds are as: V-3d ($4s^2$ $3d^3$), Mn-3d ($4s^2$ $3d^5$), and Ni-3d ($4s^2$ $3d^2$). Crystal field theory illustrates the splitting of these M-3d states into d-t_{2g} and d-e_g levels. For V-based perovskites, the configuration is $3t_{2g}$ ($\uparrow$), $0e_g$ ($\uparrow$), $0t_{2g}$ ($\downarrow$), and $0e_g$ ($\downarrow$); for Mn-based perovskites, it is $3t_{2g}$ ($\uparrow$), $2e_g$ ($\uparrow$), $0t_{2g}$ ($\downarrow$), and $0e_g$ ($\downarrow$); and for Ni-based perovskites, it is $2t_{2g}$ ($\uparrow$), $0e_g$ ($\uparrow$), $0t_{2g}$ ($\downarrow$), and $0e_g$ ($\downarrow$) adhering to the Hund's rule.

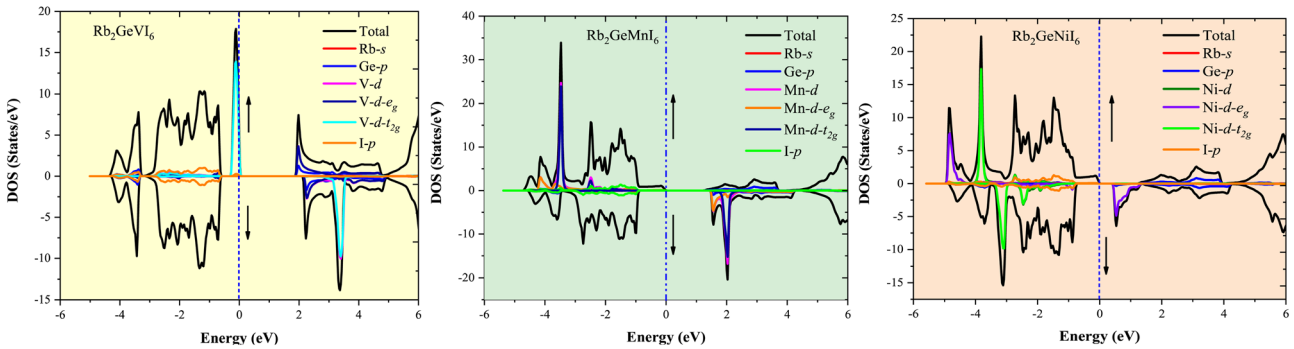

Fig. 7 Graphical representation of total density of states (TDOS) and projected density of states (PDOS) for Rb_2GeMX_6 (M = V, Mn, Ni) double perovskites determined *via* GGA + mBJ approach.

Since each unpaired electron contributes $1\mu_B$ to the net magnetization, the total spin moments align perfectly with the calculated values of $3\mu_B$, $5\mu_B$, and $2\mu_B$ for V, Mn, and Ni-based compounds, respectively. Furthermore, these results suggest a high degree of spin polarization at the Fermi level, reinforcing their potential for generating spin polarized currents. Given their pronounced magnetic properties, these materials hold significant promise for spintronic applications and other advanced technologies relying on spin based electronic mechanisms.

The Curie temperature (T_C), the threshold at which a ferromagnetic material undergoes a transition to a paramagnetic state, is determined for the Rb_2GeMI_6 compounds using the mean field approximation (MFT) within the Heisenberg model. This calculation follows the relation:[20,62] $T_C = \frac{2\Delta E}{3xK_B}$, where ΔE represents the energy difference between the ferromagnetic (FM) and antiferromagnetic (AFM) states, k_B denotes the Boltzmann constant, and x corresponds to the concentration of magnetic ions. The parameter ΔE is obtained from first principles density functional theory (DFT) calculations, wherein the total energies of FM and AFM/NM configurations are derived from total energy *versus* volume curves. The energy difference, expressed as: $\Delta E = E_{AFM/NM} - E_{FM}$, signifies the energy required to stabilize the ferromagnetic state. Given that each compound contains a single magnetic ion (V, Mn, or Ni), x assumes a value of 1. The computed values of ΔE are 0.137 eV for Rb_2GeVI_6, 0.150 eV for Rb_2GeMnI_6, and 0.114 eV for Rb_2GeNiI_6. Substituting these values into the equation yields Curie temperatures of 530.39 K, 580.72 K, and 440.47 K, respectively. These values significantly surpass those typically observed in double perovskite oxides, revealing the strength of the ferromagnetic interactions present in these materials. The remarkably high Curie temperatures indicate the exceptional stability of their magnetic ordering and suggest their viability for advanced spintronic applications, where robust ferromagnetism at elevated temperatures is imperative.

To elucidate the origin of the elevated Curie temperatures in these halide double perovskites compared to their oxide counterparts, we conduct a comparative analysis between Rb_2GeMI_6 and Bi_2CrOsO_6. The findings indicate that the remarkably high T_C in halide perovskites arises from an indirect exchange coupling mechanism mediated by Ge-I_6 octahedral units, facilitating interactions between transition metal ions. As depicted in Fig. 7, a strong hybridization is observed between M (V, Mn, Ni)-3d and I-4p orbitals, attributed to a 90° quasi-super exchange interaction between M-3d and the Ge-I_6 σs–p* orbitals. This contrasts sharply with the exchange mechanism in double perovskite oxides, where a 180° super exchange interaction involving Cr(d)–O(p)–Os(d) orbitals predominates. The 90° exchange pathway proves to be significantly more effective in stabilizing ferromagnetism, consistent with the Pauli exclusion principle.

The ferromagnetic ground state, established through total energy *vs.* volume graphs (Fig. 2), is further validated by magnetic susceptibility calculations. Using the BoltzTraP code,[39] which employs semiclassical Boltzmann theory, we compute susceptibility as a function of temperature and extract the Curie–Weiss model parameters by fitting the equation $\chi = \frac{C}{T - \Theta}$.[63] In this equation, χ represents the magnetic susceptibility, C is the Curie constant, a material-specific parameter related to the magnetic moment, T is the absolute temperature in Kelvin, and Θ is the Weiss temperature, which characterizes the nature of magnetic interactions—where a positive Θ signifies predominant ferromagnetic interactions, while a negative Θ suggests antiferromagnetic ordering. The Curie constant (C) is determined from the slope of the linear fit in the high-temperature paramagnetic region of the $1/\chi$ *vs.* T plot, while the Weiss temperature (Θ) is obtained as the intercept where $1/\chi$ extrapolates to zero. As illustrated in Fig. 8, the inverse susceptibility curves yield positive Θ values of approximately 98 K for Rb_2GeVI_6, 90 K for Rb_2GeMnI_6, and 95 K for Rb_2GeNiI_6. These positive values unequivocally confirm the dominance of ferromagnetic interactions, in full agreement with Curie–Weiss behavior.[63] Consequently, we establish that the ground state of Rb_2GeMI_6 (M = V, Mn, Ni) is intrinsically ferromagnetic, reinforcing the robustness of their magnetic ordering and highlighting their potential for applications in advanced spintronics.

3.6 Electron charge density distribution

The electronic charge density analysis offers valuable insights into the chemical stability and bonding characteristics of materials. In Fig. 9, we present the spin-polarized charge density plot of Rb_2GeVI_6 along the (111) plane, with similar

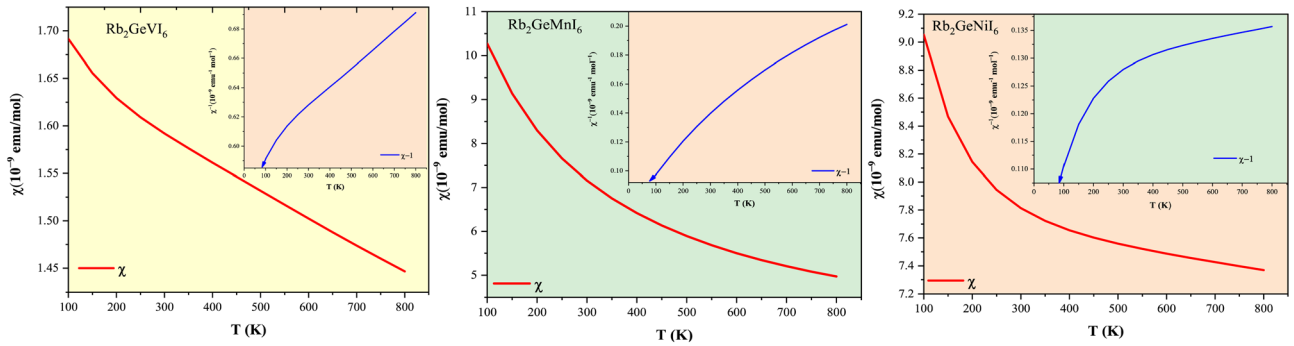

Fig. 8 Plot of magnetic susceptibility (χ) and its reciprocal (χ^{-1}) against temperature for Rb_2GeMI_6 (M = V, Mn, Ni) halide perovskites.

patterns observed in other compounds, thus omitting them for brevity. The graphical plot highlights concentrated electron cloud density at atomic positions, a key indicator of bonding interactions within the lattice. Following Pauling's theory, a chemical bond is formed when the bonding force between atoms is particularly strong. The electron clouds around Rb and I atoms are predominantly spherical, suggesting an ionic bonding character, with Rb as the electropositive donor and I as the electronegative acceptor. In contrast, the bonding between Ge/V and I atoms demonstrates clear covalent characteristics, as evidenced by the dumbbell-shaped electron clouds along the Ge/V–I bonds, indicating charge sharing between the atoms. This covalent interaction is further confirmed by the overlapping electron density contours. The overall bonding analysis reveals a distinct hybridization of ionic and covalent bonds, highlighting the material's polar covalent bonding nature, which plays a crucial role in its structural and chemical stability.

3.7 Thermoelectric coefficients

The thermoelectric effect, enabling the seamless interconversion of thermal and electrical energy, is governed by the dimensionless figure of merit (zT), defined by: $zT = \frac{S^2\sigma}{\kappa}T$ where S is the Seebeck coefficient, σ is the electrical conductivity, κ is the thermal conductivity, and T is the temperature. This equation highlights the dual strategy for maximizing thermoelectric performance—boosting the power factor ($S^2\sigma$) while suppressing heat flow (κ). Herein, we applied semi-classical Boltzmann transport theory under the rigid band and constant relaxation time (τ) approximations, using BoltzTraP code[39] to extract these parameters. The relaxation time, τ, a measure of the interval between electron scattering events, assumes minimal variation across the thermal energy range, simplifying the expressions for electrical conductivity (σ/τ), electronic thermal conductivity (κ_e/τ), and figure of merit (zT).

In this study, we analyzed the thermoelectric coefficients as functions of temperature and chemical potential, as illustrated in Fig. 10(a)–(d) and 11(a)–(c). Given the intrinsic ferromagnetism of the investigated materials, a spin-polarized perspective is essential, as charge and heat transport arise from distinct contributions of spin-up (↑) and spin-down (↓) states. To quantify the net effect, we employed the two-current model, a widely adopted framework for describing spin-dependent transport in ferromagnetic materials. Within this formalism, the total electrical conductivity is expressed as: $\sigma = \sigma(\uparrow) + \sigma(\downarrow)$. Similarly, the electronic thermal conductivity follows: $\kappa_e = \kappa_e(\uparrow) + \kappa_e(\downarrow)$, the net Seebeck coefficient, incorporating contributions from both spin states, is given as:[42] $S = \frac{S(\uparrow)\sigma(\uparrow) + S(\downarrow)\sigma(\downarrow)}{\sigma(\uparrow)\sigma(\downarrow)}$. Here, $S(\uparrow)$, $S(\downarrow)$ denote the Seebeck coefficients for spin-up and spin-down states, respectively, $\kappa_e(\uparrow)$ and $\kappa_e(\downarrow)$ correspond to the thermal conductivity for the up and down spin directions, respectively, and $\sigma(\uparrow)$ and $\sigma(\downarrow)$ represent the corresponding electrical conductivities.

The detailed analysis of thermoelectric coefficients in relation to temperature (200 K to 800 K) and chemical potential (−2 eV to 2 eV) is provided below.

3.7.1 Seebeck coefficient. Thermoelectric materials are recognized for their ability to convert temperature differences into electric voltage, governed by the Seebeck effect. This effect, quantified by the Seebeck coefficient (S), is expressed through the equation $\Delta V = S\Delta T$, where ΔV is the voltage and ΔT represents the temperature gradient. The efficiency of this conversion is heavily influenced by carrier dynamics and scattering processes within the material.

The variation of S with temperature for Rb_2GeVI_6, Rb_2GeMnI_6, and Rb_2GeNiI_6 is depicted in Fig. 10(a). At lower temperatures (100 K), these materials exhibit remarkably high S values, recorded at 600 μV K^{-1}, 550 μV K^{-1}, and 450 μV K^{-1}, respectively. However, with increasing temperature, the coefficients decline, reducing to approximately 275 μV K^{-1}, 260 μV K^{-1}, and 250 μV K^{-1} by 750 K. This reduction stems from the temperature-driven excitation of electrons. As thermal energy increases, electrons transition from the valence band to the conduction band, creating electron–hole pairs. Consequently, the increased carrier concentration reduces S. The relationship between S and carrier concentration (n) can be represented as:[42] $S = \frac{8\pi^2 k_B^2}{3e\hbar^2} m^* T \left(\frac{\pi}{3n}\right)^{2/3}$ where m^* is the effective carrier mass, k_B is Boltzmann's constant, and T is the temperature. At absolute zero, semiconductors lack free carriers, theoretically resulting in an infinite S. However, as temperature rises, thermal excitation generates carriers, diminishing S.

In addition to temperature, we also examine the chemical potential dependency of the Seebeck coefficient. The chemical potential (μ) is a crucial factor in influencing both the magnitude and the polarity of the Seebeck coefficient, as it determines the distribution of charge carriers at elevated temperatures (S). Fig. 11(a) examines the behavior of S across a range of chemical potentials for various temperatures. Positive S values signify p-type conduction (hole carriers), whereas negative values indicate n-type behavior (electron carriers). Peaks in S emerge in regions of low carrier concentration, typically between 0–1.5 eV, where the density of states (DOS)

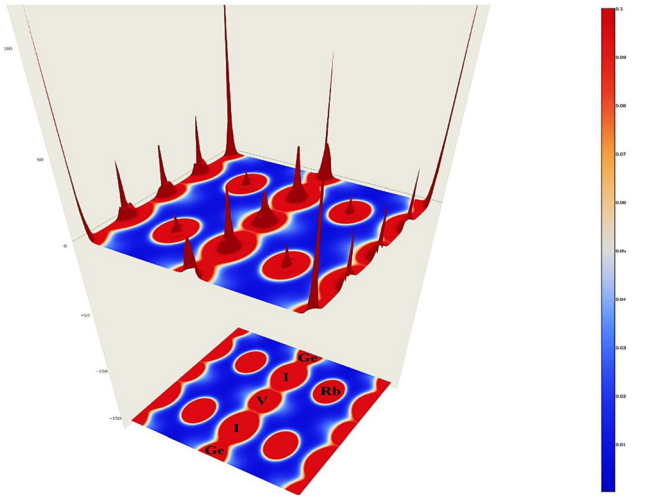

Fig. 9 Design of electronic charge density of Rb_2GeVI_6 halide perovskite.

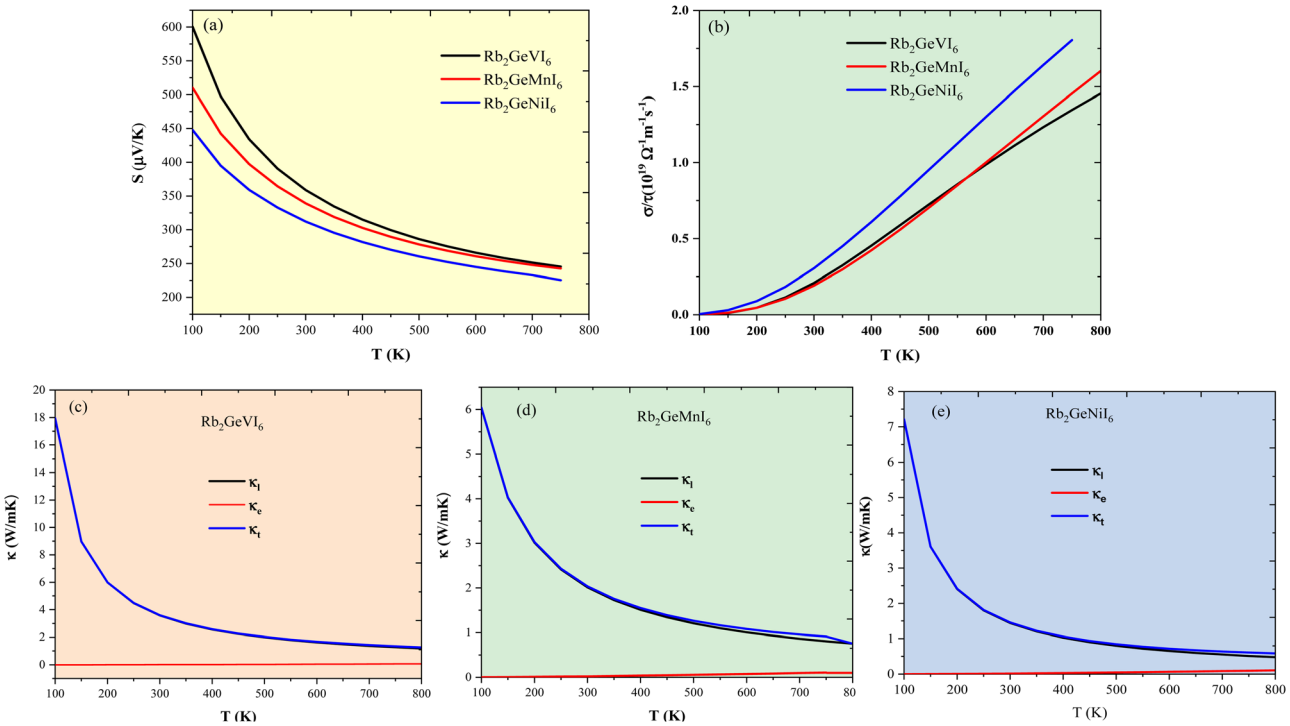

Fig. 10 Temperature variations for (a) Seebeck coefficient (S), (b) electrical conductivity (σ/t), (c)–(e) lattice, electronic and total thermal conductivity (κ_e, κ_l, κ_t) of Rb_2GeMI_6 halide perovskites.

is sparse. Conversely, high DOS regions, where carrier concentration is substantial, show diminished S. For instance, at room temperature, S reaches values of ± 3000 μV K^{-1} for Rb_2GeVI_6, ± 2000 μV K^{-1} for Rb_2GeMnI_6, and ± 700 μV K^{-1} for Rb_2GeNiI_6. The superior performance of Rb_2GeVI_6 is attributed to its larger band gap, which sustains high S values by limiting carrier generation. The computed values of the Seebeck coefficient (S) are presented in Table 7 alongside data for similar materials,[27,30] with these compounds exhibiting higher S values than those previously reported, thereby underscoring their superior thermoelectric performance.

To gain further insight, we analyze the variations of the Seebeck coefficient in conjunction with the density of states (DOS) and carrier concentration as functions of chemical potential for Rb_2GeVI_6. This analysis distinctly focuses on the spin-up and spin-down channels, as depicted in Fig. 12, while similar trends in other compounds are omitted for clarity. The spin-up channel displays prominent peaks in the Seebeck coefficient between 0 and 1.0 eV, while the spin-down channel shows significant peaks within the narrower range of 0 to 0.5 eV. This behavior arises from the reduced electronic population (DOS) in these specific regions, which limits the number of charge carriers, intensifies the energy dependence of transport, and consequently enhances the Seebeck coefficient. These peaks illustrate the critical interplay between electronic band structure and carrier transport properties. At elevated temperatures (800 K), the peak Seebeck coefficients decline to ± 1000 μV K^{-1} for Rb_2GeVI_6, ± 900 μV K^{-1} for Rb_2GeMnI_6, and ± 300 μV K^{-1} for Rb_2GeNiI_6. This reduction aligns with the Mott relation, which links Seebeck coefficient to chemical potential and temperature:[64] $S = \frac{\pi^2 k_B^2 T}{3e}\left\{\frac{1}{n}\frac{dn(\varepsilon)}{d\varepsilon} + \frac{1}{\mu}\frac{dn(\varepsilon)}{d\varepsilon}\right\}_{\varepsilon=\mu}$. As temperature rises, both types of carriers (electrons and holes) are thermally activated, leading to a bipolar effect that reduces S. However, due to the relatively large band gaps (>0.64 eV), these materials avoid complete cancellation of S, maintaining non-zero values even at high temperatures. This makes them highly promising for applications in thermoelectric generators, coolers, thermocouples, and temperature sensors.

3.7.2 Electrical conductivity. Electrical conductivity (σ/τ) characterizes a material's ability to transport charge carriers. To gain deeper insight, we first examine the temperature-dependent variation of the electrical conductivity coefficient (σ/τ) in Rb_2GeMI_6 double perovskites, as depicted in Fig. 10(b). With rising temperature, electrical conductivity (σ) steadily increases, driven by a reduction in electrical resistance—a hallmark characteristic of semiconducting materials. Beginning at 200 K, σ follows a consistent upward trajectory, peaking at 800 K, where it attains values of 1.4×10^{19} (Ω^{-1} m^{-1} s^{-1}) for Rb_2GeVI_6, 1.5×10^{19} (Ω^{-1} m^{-1} s^{-1}) for Rb_2GeMnI_6 and 1.75×10^{19} (Ω^{-1} m^{-1} s^{-1}) for Rb_2GeNiI_6. The fundamental mechanism behind this conductivity enhancement lies in the relation $\sigma = ne\mu$, where n is the carrier concentration, e is the elementary charge, and μ represents carrier mobility.[42] At absolute zero, these perovskites behave as insulators, with fully occupied states below the Fermi level preventing electrical conduction.

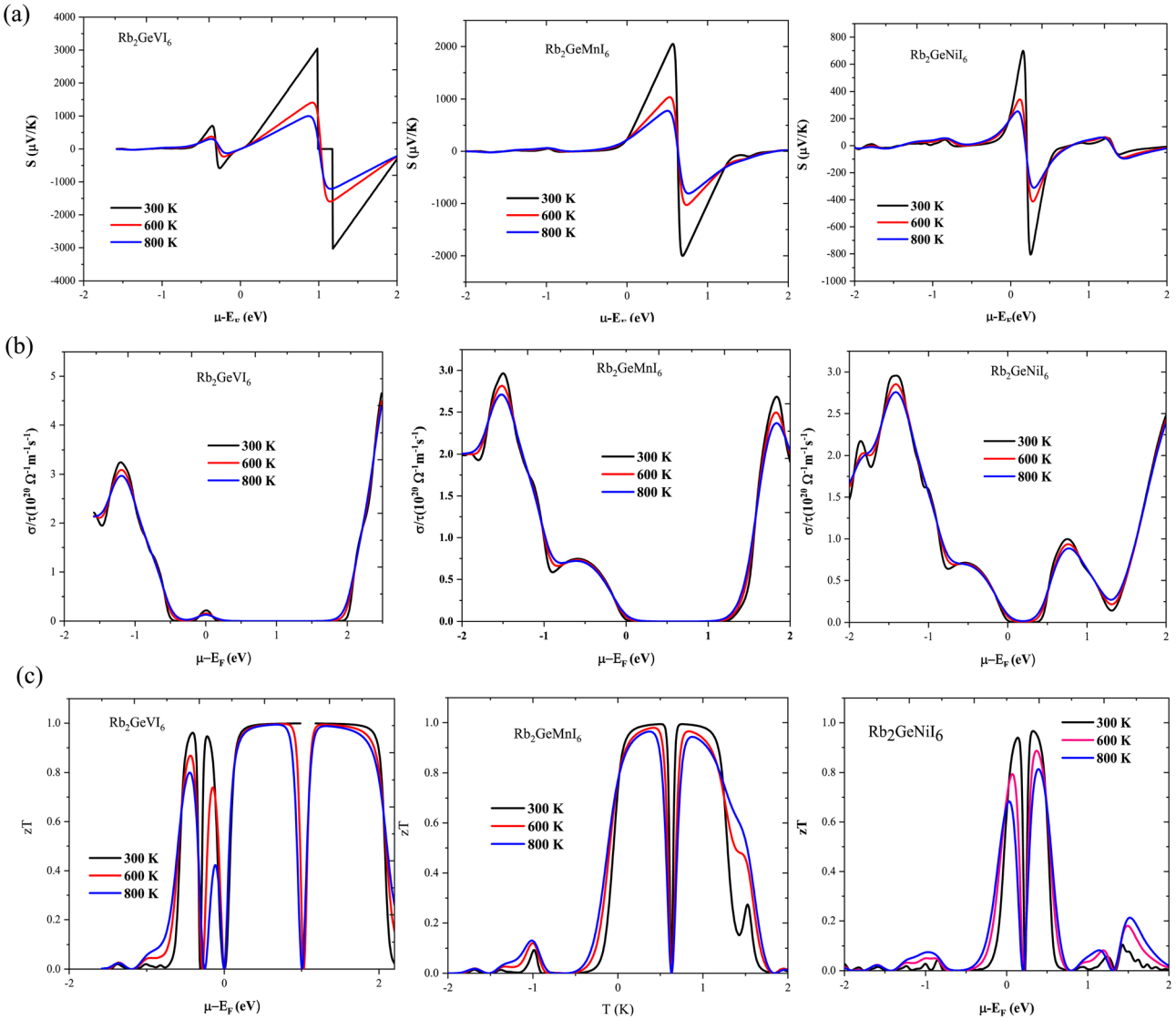

Fig. 11 Thermoelectric plots of (a) Seebeck coefficient (S), (b) electrical conductivity (σ/t), and (c) figure of merit (zT) against chemical potential at different temperatures (300 K, 600 K, 800 K) for Rb_2GeMI_6 (M = V, Mn, Ni) halide perovskites.

However, as thermal energy increases, electrons are excited into the conduction band (CB), forming electron–hole pairs and consequently amplifying carrier concentration. The extent of this thermal activation is directly linked to the band gap of each material, with larger band gaps requiring greater energy input to facilitate electronic transitions. Among the three compounds, Rb_2GeNiI_6 exhibits the highest electrical conductivity, a consequence of its smaller band gap, which enables more efficient charge carrier generation compared to Rb_2GeMnI_6 and Rb_2GeVI_6.

Table 7 Calculated thermoelectric and optical parameters for Rb_2GeMI_6 (M = V, Mn, Ni) halide perovskites in comparison with other theoretical results

	Thermoelectric parameters (300 K)		Optical parameters (0–5 eV)	
Material	Seebeck coefficient (μV K^{-1})	Figure of merit (zT)	Real part $\varepsilon_1(\omega)$	Imaginary part $\varepsilon_2(\omega)$
Rb_2GeVI_6	3000	1.00	8.0	6.0
Rb_2GeMnI_6	2000	0.99	8.4	4.9
Rb_2GeNiI_6	700	0.97	8.6	5.5
$Rb_2ScAuBr_6$[27]	150	0.61	5.0[28]	3.0[28]
Rb_2ScAuI_6[27]	165	0.82	4.9[28]	2.5[28]
$Cs_2AgBiCl_6$[30]	236	0.74	5.2	3.5
$Cs_2AgBiBr_6$[30]	234	0.73	7.0	5.5

The effect of chemical potential on electrical conductivity across different temperatures is visualized in Fig. 11(b), which maps σ/τ at 300 K, 600 K, and 800 K. Across all three perovskites, conductivity peaks are prominent in the energy range of approximately −2 to 2 eV, aligning with electronic states near the Fermi level. However, a notable distinction arises in Rb_2GeVI_6, where the conductivity peaks shift slightly away from the Fermi level, reflecting its wider band gap and the correspondingly higher energy required for charge carrier excitation. Despite this displacement, states at the Fermi level, especially

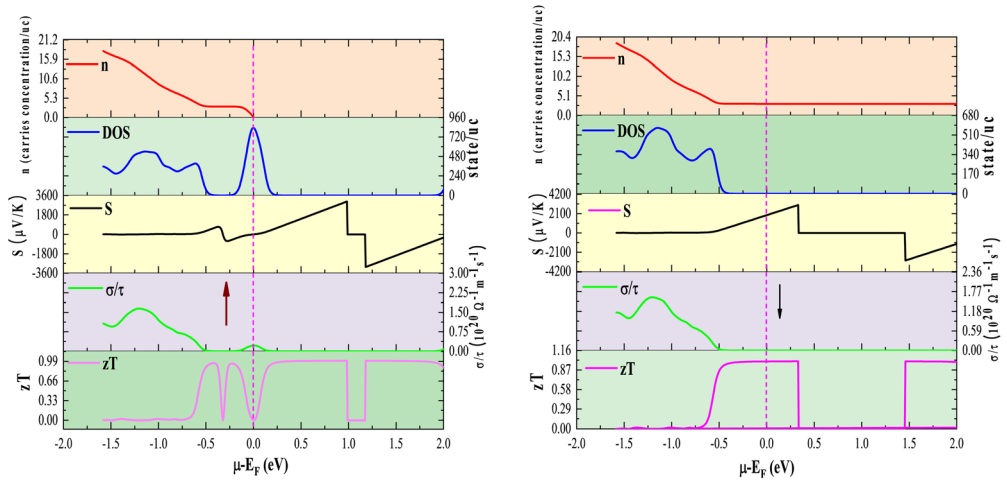

Fig. 12 Comparison of the Seebeck coefficient (S), electrical conductivity (σ/τ), figure of merit (zT), carrier concentration (n), and volumetric density of states (DOS) as a function of chemical potential at 300 K for the Rb_2GeVI_6 halide perovskite. The upward and downward arrows represent the spin-up and spin-down directions, respectively.

those from spin-up electrons contribute significantly to the material's overall electrical transport. Furthermore, secondary conductivity peaks appearing on both sides of the Fermi level highlight contributions from electronic states in both spin channels, reinforcing the role of band structure asymmetry in charge transport mechanisms.

A comparative analysis of Fig. 11(a) and (b) unveils a striking inverse relationship between electrical conductivity and the Seebeck coefficient. This interplay is governed by their fundamental dependence on carrier concentration: while σ scales proportionally with n, the Seebeck coefficient exhibits an inverse dependence.[42] Consequently, regions exhibiting conductivity peaks correspond to minima in the Seebeck coefficient, and *vice versa*.

To gain deeper insight into the interplay between electrical conductivity and chemical potential, we map the variations of total electrical conductivity (σ/τ), carrier concentration (n), and volumetric density of states (DOS) as functions of chemical potential at 300 K, with a focused examination of Rb_2GeVI_6 for clarity. As shown in Fig. 12, these plots reveal that carrier concentration sharply decreases near the pseudo-gap in the band structure, a phenomenon that significantly contributes to the observed peaks in the Seebeck coefficient. Conversely, conductivity peaks materialize at chemical potentials where the DOS is highest, indicating that densely packed electronic bands provide an ample supply of charge carriers, thereby enhancing conduction efficiency.

3.7.3 Thermal conductivity. The thermoelectric efficiency of materials is intrinsically tied to their thermal conductivity (κ), which governs heat transport through both charge carriers and lattice vibrations. A key requirement for high-performance thermoelectric devices is the suppression of thermal conductivity to sustain a strong temperature gradient, thereby maximizing thermoelectric voltage generation. Thermal transport in solids comprises two principal components: the electronic contribution (κ_e), which arises from charge carrier dynamics, and the lattice contribution (κ_l), driven by phonon-mediated heat transfer. The temperature-dependent evolution of κ_e, κ_l, and total thermal conductivity (κ_t) for the investigated perovskites is detailed in Fig. 11(c)–(e), providing critical insight into their heat conduction mechanisms. As temperature increases, κ_e follows an upward trajectory due to enhanced charge carrier mobility, a trend characteristic of thermoelectric materials with metallic-like conduction behavior. In contrast, κ_l, estimated *via* Slack's model,[65,66] exhibits a decreasing trend with temperature, driven by intensified phonon–phonon scattering at elevated thermal energies.

Slack's theoretical framework describes κ_l as a function of structural and anharmonic properties, encapsulated in the expression:[65,66] $\kappa_l = \dfrac{A\theta_D^3 V^{1/3} m}{\gamma^2 N^{2/3} T}$, where θ_D denotes the Debye temperature, γ represents the Gruneisen parameter, V is the molar volume, m is the average molar mass per atom, N is the number of atoms in the unit cell, and T is the absolute temperature. The parameter A, which depends on the anharmonicity of the lattice, is given by:[65] $A = \dfrac{2.43 \times 10^8}{1 - \dfrac{0.514}{\gamma} + \dfrac{0.228}{\gamma^2}}$. The model indicates that κ_l is influenced by structural properties such as atomic masses, lattice geometry, and anharmonic phonon interactions. As shown in Fig. 10(c)–(e), the decrease in κ_l with temperature can be attributed to enhanced phonon scattering at higher thermal energies. At 300 K, Rb_2GeVI_6, Rb_2GeMnI_6, and Rb_2GeNiI_6 exhibit lattice thermal conductivity values of 3.10 W m^{-1} K^{-1}, 2.05 W m^{-1} K^{-1}, and 1.57 W m^{-1} K^{-1}, respectively. These relatively low κ_l values are attributed to the complex structural frameworks of these materials, characterized by ten atoms per unit cell and cage-like geometries. These structures facilitate significant phonon scattering, often referred to as the "phonon rattling effect", resulting in lower lattice thermal conductivity.[32,33] Below 300 K, κ_l is the dominant contributor to total thermal conductivity. However, as the temperature rises toward 800 K, κ_l diminishes sharply, while κ_e increases due to the enhanced thermal energy of carriers.

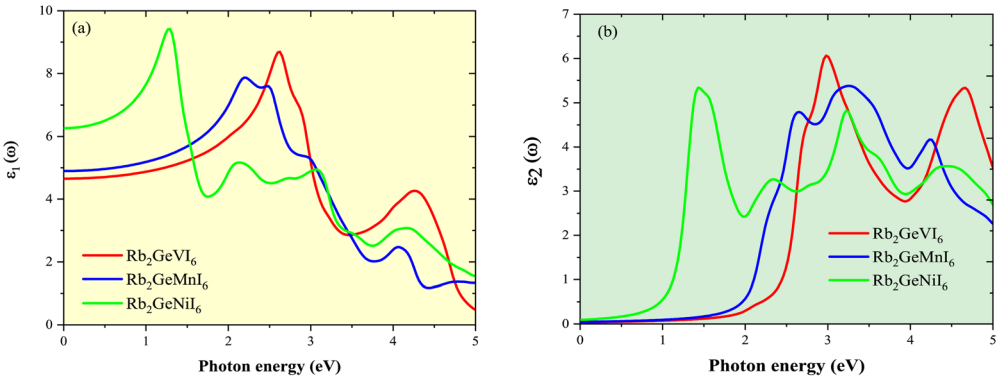

Fig. 13 Plot of the dielectric constant (a) real part ($\varepsilon_1(\omega)$) and (b) imaginary part ($\varepsilon_2(\omega)$) against photon energy for Rb_2GeMI_6 halide perovskites.

Consequently, at elevated temperatures, κ_t becomes primarily governed by the electronic contribution. The overall low thermal conductivity values of these Rb-based double perovskites highlight their suitability for thermoelectric applications. Their ability to maintain low κ_t, even at high temperatures, makes them highly promising candidates for waste heat recovery and energy harvesting technologies.

3.7.4 Figure of merit (zT). The thermoelectric figure of merit, zT, serves as a fundamental gauge for assessing the efficiency of materials in energy conversion processes. A systematic evaluation of zT as a function of chemical potential and temperature, as depicted in Fig. 11(c), reveals critical insights into the transport properties of Rb_2GeMI_6 halide perovskites. The plot demonstrates that the zT values for all three materials attain peak magnitudes approaching unity, with these maxima located in the immediate vicinity of the Fermi level. This precise alignment underscores the critical role of the electronic band structure in dictating and optimizing thermoelectric performance. However, as temperature escalates, a dual mechanism—comprising a declining Seebeck coefficient and increasing thermal conductivity—leads to a downturn in zT, a well-documented trend in thermoelectric physics. At 300 K, the zT values of Rb_2GeVI_6 (1.00), Rb_2GeMnI_6 (0.99), and Rb_2GeNiI_6 (0.97) highlight their exceptional thermoelectric efficiency. This superior performance is attributed to their intrinsically ultralow thermal conductivity, which minimizes heat dissipation, and a high Seebeck coefficient, which ensures effective charge carrier diffusion. Among the three, Rb_2GeVI_6 exhibits the highest zT, a consequence of its wider band gap, which enhances carrier energy filtering, thereby bolstering its thermoelectric output. When benchmarked against existing materials in the literature,[27,30] as presented in Table 7, these halide perovskites exhibit a superior thermoelectric figure of merit (zT), positioning them as prime candidates for next-generation energy-harvesting technologies. The maximum zT values, consistently observed within the 0–1 eV energy range, reaffirm their alignment with the Fermi level, a pivotal factor in optimizing charge carrier transport. Given their high efficiency, superior thermoelectric response, and excellent thermal insulation properties, these materials emerge as cutting-edge contenders for sustainable thermoelectric applications, with potential extending to waste heat recovery, renewable energy harvesting, and solid-state cooling technologies, marking a significant leap forward in the field of thermoelectric materials.

A deeper examination of the exceptional thermoelectric properties of Rb_2GeVI_6, along with strategies for further optimization, necessitates a comparative analysis of its density of states (DOS), carrier concentration (n), and zT at 300 K, considering both spin-up and spin-down channels, as illustrated in Fig. 12. Given the consistent trends observed across all three studied materials, we present a representative plot for Rb_2GeVI_6, while omitting the others for brevity. Notably, distinct peaks in the thermoelectric figure of merit (zT) are consistently observed within the energy ranges of approximately −0.5 to 1 eV for the up-spin channel and −0.5 to 0.5 eV for the down-spin channel, an outcome intrinsically linked to the modulation of electronic states in the density of states (DOS). This suppression of electronic states leads to a concomitant reduction in carrier concentration within this energy regime, a phenomenon that plays a pivotal role in enhancing thermoelectric efficiency. A diminished p(n)-type carrier concentration contributes to an amplified Seebeck coefficient (S), a key determinant of thermoelectric voltage, which directly influences the elevation of zT values. Despite these remarkable thermoelectric properties, additional enhancement remains within reach through strategic material engineering approaches. The application of external strain or the refinement of hole-doping methodologies, as previously proposed in the literature,[67] presents compelling avenues for further optimization. By tailoring these factors, it is possible to fine-tune the electronic band structure, thereby reinforcing the Seebeck coefficient while concurrently maintaining low thermal conductivity. Such advancements would unlock even greater thermoelectric efficiency, solidifying halide perovskites as frontrunners in next-generation energy conversion technologies.

3.8 Dielectric optical properties

The optical response of a material is fundamentally governed by its band structure and dielectric function, $\varepsilon(\omega) = \varepsilon_1(\omega) + i\varepsilon_2(\omega)$, where $\varepsilon_1(\omega)$ represents the real component dictating dispersion and charge screening, while $\varepsilon_2(\omega)$ corresponds to the imaginary component associated with optical absorption. These components adhere to the Kramer's–Kronig relations, ensuring their interdependence.[61] The static dielectric constant, a key parameter

influencing charge transport, is directly affected by the band gap. The analysis of the real dielectric function $\varepsilon_1(\omega)$ as a function of photon energy, as shown in Fig. 13(a), indicates that Rb_2GeNiI_6 exhibits a higher static dielectric constant, primarily due to its lower band gap. A reduced band gap lowers the energy barrier for charge transport, thereby enhancing carrier screening and mitigating defect-induced scattering. The spectral variation of $\varepsilon_1(\omega)$ shows an increasing trend with photon energy. Notably, Rb_2GeNiI_6 attains a peak dielectric constant of $\sim$8.6 at 1.0 eV, whereas Rb_2GeMnI_6 and Rb_2GeVI_6 reach maxima of 8.0 and 8.4 at 2.0 eV and 2.5 eV, respectively. The absorptive behavior characterized by $\varepsilon_2(\omega)$ provides insights into electronic transitions, as depicted in Fig. 13(b). The spectra of $\varepsilon_2(\omega)$ against photon energy for Rb_2GeMI_6 reveal distinct peaks attributed to inter-band transitions, predominantly from I-5p valence states to M-d conduction states within the visible range. A secondary set of transitions, occurring between 3.5–5.0 eV, is associated with excitations from I-5p valence bands to Ge-p conduction bands, positioned away from the Fermi level. Rb_2GeNiI_6 exhibits a strong absorption peak ($\sim$5.5) at 1.5 eV, indicating efficient visible-light interaction, while Rb_2GeVI_6 and Rb_2GeMnI_6 show peaks at 3.0 eV and 2.5 eV, respectively, at higher photon energies due to their larger band gaps, with corresponding maximum values of 6.0 and 4.9. Table 7 compiles all data related to the dielectric constant, along with results from similar compounds for comparison. Our findings demonstrate superior performance compared to previous studies,[28,30] highlighting the potential of inorganic Rb_2GeMI_6 perovskites as promising alternatives to lead-halide perovskites in optoelectronic and photovoltaic applications, owing to their favourable dielectric properties and strong visible-light absorption.

4. Conclusion

To conclude, we conducted a comprehensive evaluation of the structural, electronic, magnetic, and thermoelectric properties of Rb_2GeMI_6 (M = V, Mn, Ni) halide perovskites. Structural optimization confirms the stability of these compounds in the ferromagnetic phase, corroborated by positive Curie–Weiss constants. Mechanical stability evaluations, tolerance factor analyses, and negative enthalpy of formation further substantiate the robustness of the $Fm\bar{3}m$ cubic phase. Thermodynamic vibrational analyses, encompassing vibrational internal energy, Helmholtz free energy, entropy, and specific heat, indicate stability over a broad temperature range. Phonon dispersion calculations elucidate the dynamic behavior and stability of these perovskite structures. Electronic structure calculations employing the TB-mBJ functional indicate that all three compounds exhibit ferromagnetic semiconducting behavior, with notable spin-splitting energy gap. The compounds display integer magnetic moments of $3\mu_B$ for Rb_2GeVI_6, $5\mu_B$ for Rb_2GeMnI_6, and $2\mu_B$ for Rb_2GeNiI_6, confirming their ferromagnetic ordering and potential for spintronic and magneto-electronic applications. The Curie temperatures, calculated to be 530.39 K (Rb_2GeVI_6), 580.72 K (Rb_2GeMnI_6), and 440.47 K (Rb_2GeNiI_6), demonstrate their magnetic phase phase stability well above room temperature. Electronic charge density analyses indicate a predominantly polar covalent bonding nature within these compounds. Thermoelectric evaluations reveal substantial Seebeck coefficients and diminished thermal conductivity, culminating in high thermoelectric figure of merit (zT) values of 1.00, 0.99, and 0.97 for Rb_2GeVI_6, Rb_2GeMnI_6, and Rb_2GeNiI_6, respectively. These findings underscore the promising potential of these perovskite materials in renewable energy technologies. Overall, this comprehensive study establishes Rb_2GeMI_6 (M = V, Mn, Ni) perovskites as promising candidates for spintronic devices, magneto-electronic systems, and high-efficiency thermoelectric materials, offering significant potential for next-generation solid-state and renewable energy technologies.

Data availability

The data sets generated and thereafter analysed would be available from the corresponding author upon reasonable request.

Conflicts of interest

The authors declare no competing interest.

Acknowledgements

Mudasir Younis Sofi, a recipient of the Prime Minister Research Fellowship (PMRF) award (Letter No. 3302522), wishes to express sincere gratitude to the PMRF agency (Ministry of Education (MoE), Govt. of India) for the financial support.

References

1 I. Žutić, J. Fabian and S. D. Sarma, Spintronics: Fundamentals and applications, *Rev. Mod. Phys.*, 2004, **76**(2), 323.
2 S. A. Wolf, D. D. Awschalom, R. A. Buhrman, J. M. Daughton, S. V. Molnár, M. L. Roukes, A. Y. Chtchelkanova and D. M. Treger, Spintronics: a spin-based electronics vision for the future, *Science*, 2001, **294**, 1488.
3 P. Dey, J. N. Roy, P. Dey and J. N. Roy, Spintronics Applications, *Spintronics: Fundamentals and Applications*, 2021, pp. 223–267.
4 S. Bhatti, R. Sbiaa, A. Hirohata, H. Ohno, S. Fukami and S. N. Piramanayagam, Spintronics based random access memory: a review, *Mater. Today*, 2017, **20**(9), 530–548.
5 K. L. Wang, J. G. Alzate and P. K. Amiri, Low-power non-volatile spintronic memory: STT-RAM and beyond, *J. Phys. D:Appl. Phys.*, 2013, **46**, 074003.
6 A. Telegin and Y. Sukhorukov, Magnetic semiconductors as materials for spintronics, *Magnetochemistry*, 2022, **8**(12), 173.
7 A. Mauger and C. Godart, The magnetic, optical, and transport properties of representatives of a class of magnetic semiconductors: The europium chalcogenides, *Phys. Rep.*, 1986, **141**(2–3), 51–176.

8 X. Hao, J. S. Moodera and R. Meservey, Spin-filter effect of ferromagnetic europium sulfide tunnel barriers, *Phys. Rev. B:Condens. Matter Mater. Phys.*, 1990, **42**(13), 8235.
9 T. Story, R. R. Gałazka, R. B. Frankel and P. A. Wolff, Carrier-concentration–induced ferromagnetism in PbSnMnTe, *Phys. Rev. Lett.*, 1986, **56**(7), 777.
10 U. Lüders, M. Bibes, K. Bouzehouane, E. Jacquet, J. P. Contour, S. Fusil, J. F. Bobo, J. Fontcuberta, A. Barthélémy and A. Fert, Spin filtering through ferrimagnetic $NiFe_2O_4$ tunnel barriers, *Appl. Phys. Lett.*, 2006, **88**(8), 082505.
11 U. Lüders, A. Barthelemy, M. Bibes, K. Bouzehouane, S. Fusil, E. Jacquet, J. P. Contour, J. F. Bobo, J. Fontcuberta and A. Fert, $NiFe_2O_4$: a versatile spinel material brings new opportunities for spintronics, *Adv. Mater.*, 2006, **18**(13), 1733–1736.
12 H. Ohno, A. Shen, F. Matsukura, A. Oiwa, A. Endo, S. Katsumoto and Y. Iye, (Ga, Mn) As: a new diluted magnetic semiconductor based on GaAs, *Appl. Phys. Lett.*, 1996, **69**(3), 363–365.
13 H. Munekata, H. Ohno, S. Von Molnar, A. Segmüller, L. L. Chang and L. Esaki, Diluted magnetic III–V semiconductors, *Phys. Rev. Lett.*, 1989, **63**(17), 1849.
14 A. Haury, A. Wasiela, A. Arnoult, J. Cibert, S. Tatarenko, T. Dietl and Y. M. d'Aubigné, Observation of a ferromagnetic transition induced by two-dimensional hole gas in modulation-doped CdMnTe quantum wells, *Phys. Rev. Lett.*, 1997, **79**(3), 511.
15 D. Ferrand, J. Cibert, A. Wasiela, C. Bourgognon, S. Tatarenko, G. Fishman, T. Andrearczyk, J. Jaroszyński, S. Koleśnik, T. Dietl and B. Barbara, Carrier-induced ferromagnetism in p-$Zn_{1-x}Mn_xTe$, *Phys. Rev. B:Condens. Matter Mater. Phys.*, 2001, **63**(8), 085201.
16 C. Moure and O. Peña, Recent advances in perovskites: Processing and properties, *Prog. Solid State Chem.*, 2015, **43**(4), 123–148.
17 Y. Lu, Q. Wang, L. Han, Y. Zhao, Z. He, W. Song, C. Song and Z. Miao, Spintronic Phenomena and Applications in Hybrid Organic–Inorganic Perovskites, *Adv. Funct. Mater.*, 2024, **1**, 2314427.
18 B. Náfrádi, P. Szirmai, M. Spina, H. Lee, O. Yazyev, A. Arakcheeva, D. Chernyshov, M. Gibert, L. Forró and E. Horváth, Optically switched magnetism in photovoltaic perovskite CH_3NH_3(Mn: Pb) I_3, *Nat. Commun.*, 2016, **7**, 13406.
19 M. Caid, Y. Rached, D. Rached and H. Rached, First principles study of the structural, elastic, magneto-electronic and thermoelectric properties of double perovskite Ba_2ZrFeO_6 in ferrimagnetic phase, *Comput. Condens. Matter*, 2023, e00847.
20 B. Cai, X. Chen, M. Xie, S. Zhang, X. Liu, J. Yang, W. Zhou, S. Guo and H. Zeng, A class of Pb-free double perovskite halide semiconductors with intrinsic ferromagnetism, large spin splitting and high Curie temperature, *Mater. Horiz.*, 2018, **5**, 961.
21 J. Pei, B. Cai, H. L. Zhuang and J. F. Li, Bi_2Te_3-based applied thermoelectric materials: research advances and new challenges, *Natl. Sci. Rev.*, 2020, **7**(12), 1856–1858.
22 Y. Shtern, A. Sherchenkov, M. Shtern, M. Rogachev and D. Pepelyaev, Challenges and perspective recent trends of enhancing the efficiency of thermoelectric materials on the basis of PbTe, *Mater. Today Commun.*, 2023, **9**, 107083.
23 B. Russ, A. Glaudell, J. J. Urban, M. L. Chabinyc and R. A. Segalman, Organic thermoelectric materials for energy harvesting and temperature control, *Nat. Rev. Mater.*, 2016, **1**(10), 1–4.
24 S. Kee, M. A. Haque, D. Corzo, H. N. Alshareef and D. Baran, Self-healing and stretchable 3D-printed organic thermoelectrics, *Adv. Funct. Mater.*, 2019, **29**(51), 1905426.
25 J. Mao, H. Zhu, Z. Ding, Z. Liu, G. A. Gamage, G. Chen and Z. Ren, High thermoelectric cooling performance of n-type Mg_3Bi_2-based materials, *Science*, 2019, **365**(6452), 495–498.
26 S. Hayat, M. A. Khan, M. A. Ali, A. Khan, R. A. Alshgari, S. Mohammad and S. Al-Qaisi, Investigating optical, electronic, and thermoelectric properties of X_2ScIO_6 (X = K, Rb, and Cs) double perovskite semiconductors for green energy applications, *Comput. Theor. Chem.*, 2025, **1243**, 114992.
27 A. Ayyaz, Q. Mahmood, G. Murtaza, A. A. Abd El-Moula, S. Al-Qaisi, N. Sfina and A. S. Alshomrany, Study of mechanical, optoelectronic, and thermoelectric properties of Rb_2ScAuZ_6 (Z = Br, I) for energy harvesting applications, *Inorg. Chem. Commun.*, 2024, **165**, 112520.
28 M. Caid, D. Rached, Y. Rached and H. Rached, Comprehensive exploration of halide double perovskites $Cs_2B'GeCl_6$ (B′: Zn, Cd) for affordable energy technologies: a high-throughput investigation, *Opt. Quantum Electron.*, 2024, **56**(6), 980.
29 M. Caid, D. Rached, S. Al-Qaisi, Y. Rached and H. J. Rached, DFT calculations on physical properties of the lead-free halide-based double perovskite compound $Cs_2CdZnCl_6$, *Solid State Commun.*, 2023, **369**, 115216.
30 E. Haque and M. A. Hossain, Origin of ultra-low lattice thermal conductivity in Cs_2BiAgX_6 (X = Cl, Br) and its impact on thermoelectric performance, *J. Alloys Compd.*, 2018, **748**, 63.
31 A. Pisoni, J. Jacimovic, O. S. Barisic, M. Spina, R. Gaál, L. Forró and E. Horváth, Ultra-low thermal conductivity in organic–inorganic hybrid perovskite $CH_3NH_3PbI_3$, *J. Phys. Chem. Lett.*, 2014, **5**(14), 2488–2492.
32 K. Miyata, T. L. Atallah and X. Y. Zhu, Lead halide perovskites: Crystal-liquid duality, phonon glass electron crystals, and large polaron formation, *Sci. Adv.*, 2017, **3**(10), e1701469.
33 M. Beekman, D. T. Morelli and G. S. Nolas, Better thermoelectrics through glass-like crystals, *Nat. Mater.*, 2015, **14**(12), 1182–1185.
34 P. Blaha, K. Schwarz, G. K. H. Madsen, D. Kvasnicka, J. Luitz, R. Laskowsk, F. Tran, L. Marks and L. Marks, *WIEN2k: An Augmented Plane Wave Plus Local Orbitals Program for Calculating Crystal Properties*, Techn. Universitat, Vienna, Austria, 2019, p. 287.
35 J. P. Perdew, K. Burke and M. Ernzerhof, Generalized gradient approximation made simple, *Phys. Rev. Lett.*, 1996, **77**(18), 3865.
36 D. Koller, F. Tran and P. Blaha, Improving the modified Becke–Johnson exchange potential, *Phys. Rev. B:Condens. Matter Mater. Phys.*, 2012, **85**(15), 155109.

37 T. Charpin, A Package for Calculating Elastic Tensors of Cubic Phases Using WIEN: Laboratory of Geometrix F-75252 (Paris, France) (2001).
38 A. tero-de-la-Roza, D. Abbasi-Pérez and V. Luaña, Gibbs2: A new version of the quasi-harmonic model code. II. Models for solid state thermodynamics, features and implementation, *Comput. Phys. Commun.*, 2011, **182**(10), 2232–2248.
39 G. K. Madsen and D. J. Singh, BoltzTraP. A code for calculating band-structure dependent quantities, *Comput. Phys. Commun.*, 2006, **175**(1), 67–71.
40 M. Y. Sofi, M. S. Khan, J. Ali and M. A. Khan, Unlocking the role of 3d electrons on ferromagnetism and spin-dependent transport properties in K_2GeNiX_6 (X = Br, I) for spintronics and thermoelectric applications, *J. Phys. Chem. Solids*, 2024, **192**, 112022.
41 F. D. Murnaghan, The compressibility of media under extreme pressures, *Proc. Natl. Acad. Sci. U. S. A.*, 1944, **30**(9), 244–247.
42 M. Y. Sofi, M. S. Khan and M. A. Khan, Control of spin on ferromagnetism and thermoelectric properties of K_2GeMnX_6 (X = Cl, Br, I) halide perovskites: emerging candidates for semiconductor spintronics and thermoelectric applications, *Mater. Adv.*, 2024, **5**(11), 4913–4931.
43 M. Blanco, E. Francisco and V. Luaña, GIBBS: isothermal-isobaric thermodynamics of solids from energy curves using a quasi-harmonic Debye model, *Comput. Phys. Commun.*, 2004, **158**, 57–72.
44 Q. Chen and B. Sundman, Calculation of Debye temperature for crystalline structures case study on Ti, Zr, and Hf, *Acta Mater.*, 2001, **49**, 947–961.
45 D. V. Schroeder and J. K. Pribram, An Introduction to Thermal Physics, *Am. J. Phys.*, 1999, **67**, 1284–1285.
46 P. Debye, Zur Theorie der spezifischen Warmen, *Ann. Phys.*, 1912, **344**, 789–839.
47 A. T. Petit and P. L. Dulong, Study on the measurement of specific heat of solids, *Ann. Chim. Phys.*, 1819, **10**, 395.
48 P. Giannozzi, *et al.*, QUANTUM ESPRESSO: A modular and open-source software project for quantum simulations of materials, *J. Phys.: Condens. Matter*, 2009, **21**, 395502.
49 M. Born, On the stability of crystal lattices, *Math. Proc. Cambridge Philos. Soc.*, 1940, **36**, 160.
50 W. Voigt Textbook of Crystal Physics (G.B. Teubner, 1928).
51 A. Reuss, Berechnung Der Fließgrenze von Mischkristallen Auf Grund Der Plastizitätsbedingung Für Einkristalle, *Z. Angew. Math. Mech.*, 1929, **9**, 49–58.
52 R. Hill, Te elastic behaviour of a crystalline aggregate, *Proc. Phys. Soc., London, Sect. A*, 1952, **65**, 349.
53 M. Y. Sofi, M. S. Khan and M. A. Khan, Harnessing the half-metallicity and thermoelectric insights in Cs_2AgMBr_6 (M = V, Mn, Ni) double halide perovskites: A DFT study, *Mater. Sci. Semicond. Process.*, 2025, **186**, 109023.
54 S. F. Pugh, XCII. Relations between the elastic moduli and the plastic properties of polycrystalline pure metals, *Philos. Mag.*, 1954, **45**, 823–843.
55 I. N. Frantsevich; F. F. Voronov and S. A. Bakuta, *Elastic Constants and Moduli of Elasticity of Metals and Nonmetals*, Naukova Dumka, Kiev, 1982.
56 W. Hume-rothery, Elasticity and anelasticity of metals, *Nature*, 1949, **164**(4159), 84–85.
57 S. I. Ranganathan and M. Ostoja-Starzewski, Universal elastic anisotropy index, *Phys. Rev. Lett.*, 2008, **101**(5), 055504.
58 D. M. Teter, Computational alchemy: The search for new superhard materials, *MRS Bull.*, 1998, **23**(1), 22–27.
59 Y. Tian, B. Xu and Z. Zhao, Microscopic theory of hardness and design of novel superhard crystals, *Int. J. Refract. Met. Hard Mater.*, 2012, **33**, 93–106.
60 E. Fine, L. D. Brown and H. L. Marcus, Elastic constants versus melting temperature in metals, *Scr. Metall.*, 1984, **18**, 951–956.
61 M. Y. Sofi, A. Ramzan, M. S. Khan, A. Kumar, M. R. Rather, S. A. Sofi, S. A. Khandy and M. A. Khan, Pioneering computational insights into the structural, magnetic, and thermoelectric properties of A_3XN (A = Co, Fe; X = Cu, Zn) anti-perovskites for advanced material applications, *Mater. Sci. Semicond. Process.*, 2025, **185**, 108925.
62 J. Kudrnovsky, *et al.*, Exchange interactions in III-V and group-IV diluted magnetic semiconductors, *Phys. Rev. B:Condens. Matter Mater. Phys.*, 2004, **69**, 115208.
63 Y. Takahashi, On the origin of the Curie-Weiss law of the magnetic susceptibility in itinerant electron ferromagnetism, *J. Phys. Soc. Jpn.*, 1986, **55**(10), 3553–3573.
64 M. Jonson and G. D. Mahan, Mott's formula for the thermopower and the Wiedemann-Franz law, *Phys. Rev. B:Condens. Matter Mater. Phys.*, 1980, **21**, 4223–4229.
65 G. A. Slack, Non-metallic crystals with high thermal conductivity, *J. Phys. Chem. Solids*, 1973, **34**(2), 321–335.
66 G. Qin, A. Huang, Y. Liu, H. Wang, Z. Qin, X. Jiang, J. Zhao, J. Hu and M. Hu, High-throughput computational evaluation of lattice thermal conductivity using an optimized Slack model, *Mater. Adv.*, 2022, **3**(17), 6826–6830.
67 C. W. Wu, X. Ren, G. Xie, W. X. Zhou, G. Zhang and K. Q. Chen, Enhanced High-Temperature Thermoelectric Performance by Strain Engineering in BiOCl, *Phys. Rev. Appl.*, 2022, **18**(1), 014053.